INFORMATION TO USERS

This manuscript has been reproduced from the microfilm master. UMI films the text directly from the original or copy submitted. Thus, some thesis and dissertation copies are in typewriter face, while others may be from any type of computer printer.

The quality of this reproduction is dependent upon the quality of the copy submitted. Broken or indistinct print, colored or poor quality illustrations and photographs, print bleedthrough, substandard margins, and improper alignment can adversely affect reproduction.

In the unlikely event that the author did not send UMI a complete manuscript and there are missing pages, these will be noted. Also, if unauthorized copyright material had to be removed, a note will indicate the deletion.

Oversize materials (e.g., maps, drawings, charts) are reproduced by sectioning the original, beginning at the upper left-hand corner and continuing from left to right in equal sections with small overlaps. Each original is also photographed in one exposure and is included in reduced form at the back of the book.

Photographs included in the original manuscript have been reproduced xerographically in this copy. Higher quality 6" x 9" black and white photographic prints are available for any photographs or illustrations appearing in this copy for an additional charge. Contact UMI directly to order.

UMI

A Bell & Howell Information Company
300 North Zeeb Road, Ann Arbor MI 48106-1346 USA
313/761-4700 800/521-0600

Reproduced with permission of the copyright owner. Further reproduction prohibited without permission.

Reproduced with permission of the copyright owner. Further reproduction prohibited without permission.

NOTE TO USERS

The original manuscript received by UMI contains pages with slanted print. Pages were microfilmed as received.

This reproduction is the best copy available

UMI

Reproduced with permission of the copyright owner. Further reproduction prohibited without permission.

Reproduced with permission of the copyright owner. Further reproduction prohibited without permission.

X-RAY SPECTROSCOPIC STUDIES OF SECONDARY BATTERY MATERIALS

by

Svilen Kostov

A dissertation submitted to the Graduate Faculty in
Physics in partial fulfillment of the requirements
for the degree of Doctor of Philosophy,
The City University of New York

1998

Reproduced with permission of the copyright owner. Further reproduction prohibited without permission.

UMI Number: 9908336

UMI Microform 9908336
Copyright 1998, by UMI Company. All rights reserved.

This microform edition is protected against unauthorized copying under Title 17, United States Code.

UMI
300 North Zeeb Road
Ann Arbor, MI 48103

Reproduced with permission of the copyright owner. Further reproduction prohibited without permission.

This manuscript has been read and accepted for the Graduate Faculty in Physics in satisfaction of the dissertation requirements for the degree of Doctor of Philosophy.

9/17/98 — Professor Marten denBoer, Chair of Examining Committee

Date

9/18/98 — Professor Louis Celenza, Executive Officer

Date

Professor Steven Greenbaum

Professor Godfrey Gumbs

Dr. Jim McBreen

Professor Ken Miyano

Supervisory Committee

The City University of New York

Reproduced with permission of the copyright owner. Further reproduction prohibited without permission.

Abstract

X-RAY SPECTROSCOPIC STUDIES OF SECONDARY BATTERY MATERIALS

by

Svilen Kostov

Adviser: Professor Marten denBoer

X-ray spectroscopic methods, both NEXAFS and EXAFS were used in the study of the structural and electronic properties of different types of new battery materials.

NEXAFS analysis of the spectra of $Li_{1-x}CoO2$ secondary battery cathodes revealed that the addition of Li proceeds is strongly correlated to the increase in electronic charge on the Co ion. A structural phase transition is confirmed for $x = 0.5$. The presence of Mn^{+2} is detected in the conventionally made $LiMnO_2$ cathodes but not in ones prepared according to the new ADL process.

$Li_xV_6O_{13}$ cathode material, where $0 \leq x \leq 6$, was measured using x-ray absorption, EPR and NMR techniques. The intercalation mechanism involves a conversion of V^{+5} to V^{+4} in V_6O_{13} until the composition $Li_2V_6O_{13}$ is reached. Further addition of lithium is accompanied by the conversion of V^{+4} to V^{+3} until $Li_8V_6O_{13}$ is reached. The process is complicated and involves structural phase changes and increasing structural disorder within the multi-phase system as Li concentration is increased.

Studies of $LiNi/CoO_2$ intercalation cathodes prepared by a novel sol-gel technique suggests that although the partial substitution of Co for Ni stabilizes the system by removing Ni^{+2}, a Jahn-Teller type structural distortion in the predominantly Ni^{+3} system persists.

Reproduced with permission of the copyright owner. Further reproduction prohibited without permission.

In-situ EXAFS measurements of the pyrite cathode in a new Li/CPE/FeS_2 battery showed two distinct environments of the Fe ion, which were interpreted as those of metallic Fe and residual FeS_2 at high lithium concentration, and Li2FeS_2 and residual FeS_2 at low lithium concentration. The formation of FeS was not detected.

A new type of hydrogen ion battery incorporating a $MnSO_4$*H_2O based cathode and polymer electrolyte was also studied. Heavily cycled and discharged cathodes showed an almost identical Mn local structure to that of single cycled ones. The Mn environment becomes very different in the charged cathodes, due to a highly reversible chemical change. Formation of Mn+4 at the expense of Mn+3, upon charging is an unexpected result. Mn+7 does not appear to be created in this process.

Reproduced with permission of the copyright owner. Further reproduction prohibited without permission.

ACKNOWLEDGEMENTS

I would like to express my sincerest gratitude towards Prof. Marten denBoer and Prof. Steven Greenbaum for their continuous intellectual, financial and, most importantly, moral support during the last five years.

I would also like to thank Prof. Phillip Stallworth for his engaging discussions and personal friendship, and Richard Krumm for his friendship and help in the experimental work.

I would like to acknowledge ONR and DOE for their role in funding this research.

My thanks goes out to everybody who was helpful and had patience with me in the course of the work that led to this thesis.

Reproduced with permission of the copyright owner. Further reproduction prohibited without permission.

Table of Contents

Reproduced with permission of the copyright owner. Further reproduction prohibited without permission.

Reproduced with permission of the copyright owner. Further reproduction prohibited without permission.

List of Tables

Reproduced with permission of the copyright owner. Further reproduction prohibited without permission.

List of Figures

Reproduced with permission of the copyright owner. Further reproduction prohibited without permission.

Reproduced with permission of the copyright owner. Further reproduction prohibited without permission.

Reproduced with permission of the copyright owner. Further reproduction prohibited without permission.

1.Introduction

There is a growing need to develop highly efficient and environmentally safe secondary solid state batteries as power storage devices for the present and future economy. Current research in this area of technology includes a precise analysis of the physical and chemical properties of a broad category of materials used in the experimental stages of battery design.

The basic scientific understanding and accurate characterization of newly synthesized materials in an anode-electrolyte-cathode system is very important [1]. Knowledge of the structural changes occurring in a battery component on the atomic level, at different stages of its electrochemical cycle, can give insight into the inherent possibilities or limitations of a particular material. It can also guide the optimization of the macroscopic parameters which determine battery performance. An effective means of probing the atomic structure and composition of potential battery materials is a combination of different types of spectroscopic measurements of the interaction of electromagnetic radiation with matter, each contributing a particular set of information about the system of interest.

The work described in this thesis centers on the x-ray spectroscopic study of the structure and electronic properties of newly synthesized battery materials. The work was part of a collaborative effort including nuclear magnetic resonance (NMR), electron paramagnetic resonance (EPR) spectroscopic studies. The systems which were investigated include different lithium-containing transition metal oxides for cathode applications as well as a new type of hydrogen ion battery system.

Reproduced with permission of the copyright owner. Further reproduction prohibited without permission.

1.1 Solid State Battery Basics

The battery as an electrochemical device converts the stored chemical energy in its active materials into electrical energy through an oxidation-reduction reaction. Secondary batteries are electrically rechargeable, i.e. the reaction can be reversed. Fig. 1 illustrates a typical battery during the discharge part of its cycle. It can be symbolized as $A^- /El_i /C^+$.

1. The negative electrode or anode, A^-, is oxidized in the reaction and gives up electrons to the external circuit. It should display high efficiency as a reducing agent, good conductivity, stability, ease of fabrication and low cost. Lithium has been widely used as the active part of the anode material in secondary batteries due to its low atomic mass and high reactivity. A large fraction of operational batteries incorporate lithiated carbon anodes.

2. The electrolyte, E_l, is the ionic conductor, as well as electronic insulator, the latter requirement helps in preventing self-discharge. A wide range of materials including liquids and solids, crystalline and amorphous, as well as polymer films, [2] can be used as electrolytes.

3. The cathode, C^+, is the oxidizing agent and positive electrode. It accepts electrons from the external circuit and is reduced in the process. There is also a migration of positive ions toward it. The properties of the cathode determine the

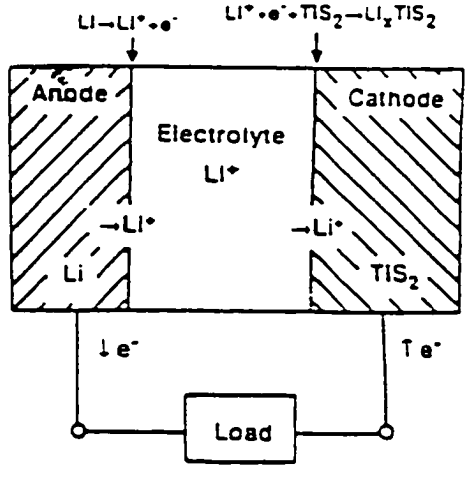

Figure 1 Schematic depiction of a Li/TiS_2 cell during the discharge part of its cycle.

Reproduced with permission of the copyright owner. Further reproduction prohibited without permission.

quality factors of a battery, since the available energy is directly related to the size and electrochemical parameters of this component. Lithiated transition metal oxides are an important class of cathode materials [3].

1.2 Secondary Lithium Battery Cathodes

The reaction of lithium and most solid inorganic compounds that could be used as cathode materials is a displacement reaction, such as the one given by Eq. 1.

$$2MO_2 + 2Li \rightarrow M_2O_3 + Li_2O \quad (1)$$

where M is a general metal. These types of reactions are non-reversible, in general, at room temperature, since they involve extensive bond breakage, new bond formation and atomic reorganization. One type of reaction, however, that is generally reversible is the *intercalation* reaction. It involves the interstitial introduction of a guest species into the framework of a host compound, with minimal or no structural modification of the host. The reversibility of intercalation suggest that it can successfully be used as a mechanism for reversible electrode reactions. The general intercalation reaction can be written as

$$A^+ + e^- + MY_n \rightleftharpoons AMY_n \quad (2)$$

where A, M, and Y are a general alkali metal, cation, and anion of the host lattice respectively. Only the M element is reduced during the intercalation process or oxidized during deintercalation. The use of lithium in this reaction at the cathode of a battery is given by the following equations

Reproduced with permission of the copyright owner. Further reproduction prohibited without permission.

$$Li^+ + e^- \rightleftharpoons Li \qquad (3.1)$$

$$xLi^+ + xe^- + MY_n \rightleftharpoons Li_xMY_n \qquad (3.2)$$

The generally accepted requirements for solid-state cathode compounds can be summarized as follows [4]:

1) Large free energy of reaction, ΔG (affording a high cell voltage)

2) Wide compositional range; that is x in Eq. 3.2 (resulting in high cell capacities).

3) High diffusivity of the guest species in the host (allowing high power densities).

4) Minimal structural change as a function of composition (resulting in a reversible reaction).

Additional desirable properties are:

1) Good electronic conductivity (to minimize resistive heat generation and eliminate the need for a conductive additive, thus reducing capacity)

2) Low solubility in the electrolyte (to prevent self-discharge).

A broad range of materials for potential use as secondary battery cathodes has been investigated. We will not attempt a full classification. Fig. 2 shows volumetric and gravimetric specific

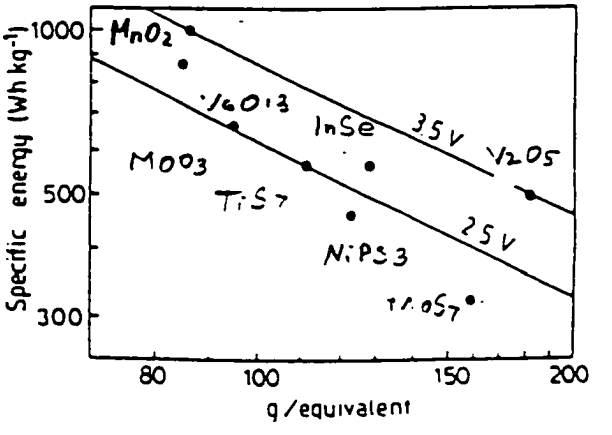

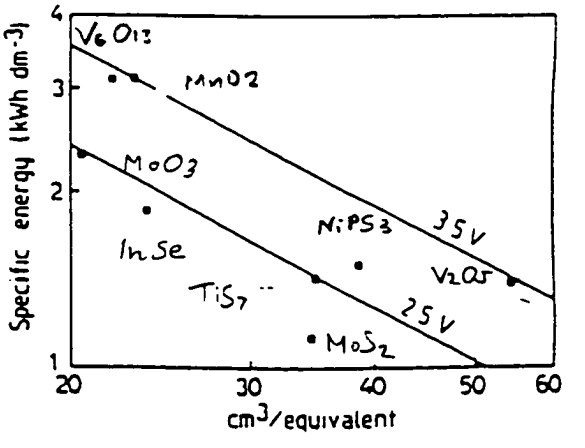

Figure 2 a)gravimetric and b)volumetric specific energies for some Li/intercalation electrode couples.

Reproduced with permission of the copyright owner. Further reproduction prohibited without permission.

energies, respectively, for different Li/intercalation electrode couples.

In the case of transition-metal oxides there is a strong ionic M-O bond. As a consequence of this, strong electrostatic repulsions exist between the intercalated Li^+ ions and the octahedral (or in some cases tetrahedral) framework cations. The spatial charge distribution is strongly modified during the intercalation/deintercalation processes, and quite often structural changes occur within the framework in order to minimize energy. The extent and range of reversibility of these changes is an important issue, since it can affect battery performance and, in cases where there is an onset of irreversible chemical changes, may lead to cell failure. The following section is intended to give a more detailed account of the most important microscopic properties of a large number of intercalation or insertion cathodes and their relationship to the macroscopic properties of battery cells.

Reproduced with permission of the copyright owner. Further reproduction prohibited without permission.

1.3 Insertion Electrodes- Physical Principles

Intercalation or insertion compounds are solids which consist of host atoms and guest atoms. The host atoms provide the lattice or framework and the guest atoms occupy sites within this framework for a period of time during the charge/discharge cycle. Two properties of intercalation compounds are important and separate them from other compounds:

1. The guests are mobile, i.e. they can move between sites in the host lattice

2. The guests can be added or removed from the host, i.e. their concentration can change.

Both of these properties are exploited in practice when intercalation compounds are used as electrodes in secondary batteries.

An example of a classical intercalation system is a graphite host and alkali metal guest atoms [5], [6] Among the many types of hosts transition metal oxide (TMO) and chalcogenides (TMC) are very important and are the main focus of this study. The main type of guest atom will be lithium, since this alkali metal has properties which make it a very good intercalant, i.e. ionic radius, atomic weight and electropositivity. The following discussion is based on Ref. 7 and gives a basic introduction to the most important aspects of atomic and electronic structure of alkali metal intercalated transition metal compounds.

In all alkali metal intercalation compounds, the guest ionizes the host, by donating its outer *s* electron to the host's electronic energy levels. Therefore there are two questions to consider: the site occupation of the guest atoms with respect to the host atoms, i.e. the geometry of arrangement, and the change in the host's electronic structure which occurs due to this site occupation.

Reproduced with permission of the copyright owner. Further reproduction prohibited without permission.

1.3.1 Sites for Ions

In a transition metal chalcogenide or oxide, positive guests like Li^+ occupy sites surrounded by negative chalcogen or oxygen ions, and distance themselves as far as possible from the positive transition metal ions. Since Li^+ has a filled outer shell of electrons, it prefers a site that is isotropic, i.e. the anions are distributed evenly around the site. For example, a Li ion would prefer a tetrahedral rather than a two dimensional square coordination. In most compounds the guest ions spend most of their time localized at a given site and only occasionally transfer to a different site by hopping. Such systems are fairly well described by lattice-gas models. This description breaks down when the guests are large enough to occupy more than one site at a time. For example, Cs in graphite is described as a liquid weakly interacting with the periodic potential of the graphite lattice [8]. The sites available for the ions depend on the structure, and there can be more than one type of site within a given structure. For example, as seen in Fig. 3a, Li can alternate between octahedral and tetrahedral sites, both existing between layers of close-packed oxygen (chalcogen) atoms. Li ions generally occupy both of these sites. There is evidence [9] that the larger Na ion occupies trigonal prismatic sites, which exist when one closed-packed layer is directly on top of another (Fig. 3b). Ionic radii are well known [10] which gives information as to whether a certain ion may occupy a particular

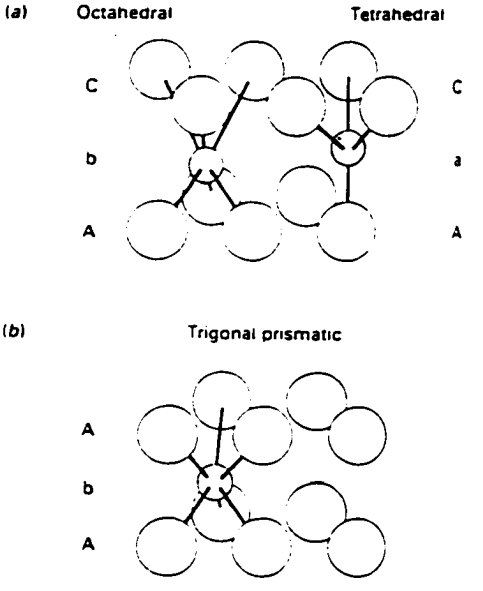

Figure 3 Sites for intercalated ions between close-packed layers of anions: a)octahedral and tetrahedral sites: b) trigonal prismatic sites

Reproduced with permission of the copyright owner. Further reproduction prohibited without permission.

site.

Host materials and their sites can be classified independently. The sites themselves span a lattice which can be one, two, or three dimensional depending on how they are connected. The host atoms can be classified according to the dimensionality of the strong bonds. Fig. 4 illustrates four different combinations geometries of site/host atoms. If the host's atoms exhibit a chainlike structure the guest can move about in all directions. This is a one dimensional host with a three dimensional lattice of guest sites. Conversely, the host can be strongly bonded in all three directions, thus allowing for tunnels of sites. Both host and sites can be layered. The last possibility is a 3D host with a 3D network of sites. The dimensionality of the host determines to some extent the types of guest that can be accommodated. For example, layered hosts can accept large guests, as well as small, i.e. large organic solvent molecules from the electrolyte together with the actual anions. Three dimensional structures do not allow such cointercalation.

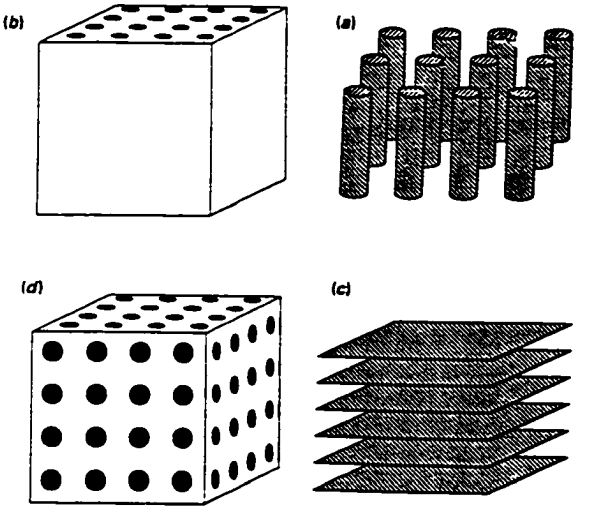

Figure 4 Schematic diagrams showing classification of host compounds: a) chains weakly bonded (1D host with 3D sites for guests; b) 3D host with 1D lattice for guests; c) layered host (2D host and 2D guest lattice); d) 3D host and 3D host lattice

Reproduced with permission of the copyright owner. Further reproduction prohibited without permission.

1.3.2 Electronic Structure

The electrons donated to the host by the guest atom occupy states that are determined by the band structure of the host lattice. In transition metal oxides or chalcogenides, electron *p* orbitals from the oxygen or chalcogen overlap with *s*, *p*, and *d* orbitals from the transition metal forming bonding and antibonding levels. The perodicity of the solid spreads these levels into bands. It is often convenient to neglect the mixed nature of the bands and label each according to the level and atom contributing most of its weight. As seen in Fig. 5a the oxygen or chalcogen *p* bands are filled and the transition metal *d* bands are empty or partially occupied. The electrons from the guests are added to the *d* bands as intercalation proceeds, so the Fermi energy moves upward relative to the bottom of the *d* bands.

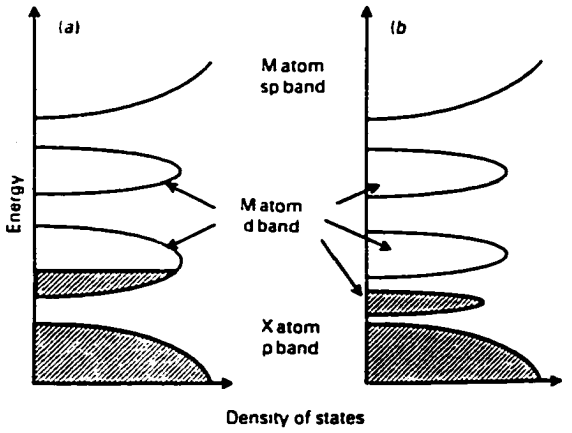

Figure 5 Schematic electron bands for transition metal oxides and chalcogenides. M is metal and X is oxygen or chalcogen

Fig. 5b shows how the *d* bands split into sub-bands. This is because the d bands are formed from antibonding combinations *d* and *p* orbitals, and those with more overlap are pushed higher in energy. The details of the splitting depend on the crystal field, i.e. how the chalcogens/oxygen coordinate the transition metal ions. For octahedral coordination, the lower band contains six states and the upper band four per transition metal, including spin up and down states. For trigonal prismatic coordination the lower band splits further and the number of state in its lowest part is two. Compounds like TiS_2 or MoO_3, where the *d* bands are empty, are semiconductors or insulators.

Reproduced with permission of the copyright owner. Further reproduction prohibited without permission.

In MoS_2, Mo contributes four of its six outer electrons to the sulfur bands, because each sulfur is two electrons short of having a full outer shell. That leaves two *d* states occupied, so the 2H form of MoS_2 in which Mo lies in a trigonal prism, is a semiconductor because the lowest *d* band is filled. The 1T form, in which Mo lies in an octahedron, is a metal because the bottom of the band splitting has disappeared. Py and Haering [11] have discussed the transformation from the 2H to the 1H form in an electrochemical cell, where the cell was prepared in the latter form. The possible cause seems to be that energy is gained when the gap between *d* states is eliminated by electron occupation of the second *d* band.

The band picture discussed so far breaks down for lighter transition metal elements (closer to the first row of the periodic table). There a more localized description is appropriate [12]. The *d* states remain more like atomic-like *d* orbitals, and the materials can be non-metallic even though the band picture indicates a partially occupied, metallic band. In this case, one may adopt an atomic description, and state that the electrons from the guest change the valence of the transition metal [13]

Another aspect of intercalation that has to be taken into account in a more complete description of the process is the effect that the charge of the intercalated ion has on the energy bands. Since the ion is closer to the oxygen/chalcogen of the host than to the transition metal, its positive charge lowers the energy of the *p* electrons relative to that of the *d* electrons. This lowering can be seen in calculations of the band structures of $LiTiS_2$ and TiS_2 [14]. The influence of the guest ions charge is greatest near the guest ion itself. When the guest atoms polarizes the chalcogen atoms around it, those in turn affect the neighboring transition metal ions by lowering the energy of their *d* states. When electrons are first added to an empty d band, this lowering can pull states out of the

Reproduced with permission of the copyright owner. Further reproduction prohibited without permission.

band, localizing electrons until the material becomes metallic at a critical concentration of electrons [15]. This so called Mott transition has been observed by electron spectroscopy in Na_xWO_3 [16].

1.3.1 Examples of Different Host Compounds

The following a is brief account of some host compounds classified according to Fig. 4. For a more complete description of different types of structures relevant to intercalation chemistry one should consult references on inorganic structural chemistry.

1.3.1.1 One dimensional host, three dimensional lattice of sites

These host consist of chains weakly bonded to one another. Examples are compounds of Mo and Se in which cubes of Mo and Se are arranged in chains and can accommodate guest ions between the chains [17]. Others have shown that it is possible to remove the intercalated ions and separate the chains in solution [18]. Some organic compounds like polyacetylene, although outside the scope of this work, are also important examples of this class of intercalation compounds.

1.3.1.2 Three dimensional structure, one dimensional tunnels

In many TMOs the transition metal ions are octahedrally coordinated by oxygen, with the octahedra joined along one direction to form chains. Octahedra belonging to different chains may share an oxygen atom, in which case we say that they are sharing corners. The tunnels that occur

Reproduced with permission of the copyright owner. Further reproduction prohibited without permission.

between the octahedra may be classified according to the number of ochahedra that span each side of the formed rectangular cross-section as shown in Fig. 6a.

Many layered compounds consist of close-packed oxygen or chalcogen anions, with transition metal ions occupying octahedral or trigonal prismatic sites (Fig. 6b). Adjacent layers of these anions are weakly coupled, and therefore various sizes guest ions can be inserted in between them. Layered compounds are usually described in terms of ABC notation, indicating the stacking sequence. From Fig.6b we see that an octahedral sandwich can be denoted as AbC, where A is the "upper" layer of oxygen/chalcogen, C is the "lower" one, and b indicates the interstitial ion. In the same manner, AbA indicates a stacking sequence in which there is a trigonal prism intercalation site. As an example, consider the well known structure of Li_xTiS_2. For values of $x < 1$, both Li and Ti are octahedrally coordinated by S. In the ABC notation the structure can be written as AbC(b)AbC where (b) denotes the lithium ions. This is the 1T form of this structure, because it has trigonal symmetry and a single layer per unit cell.

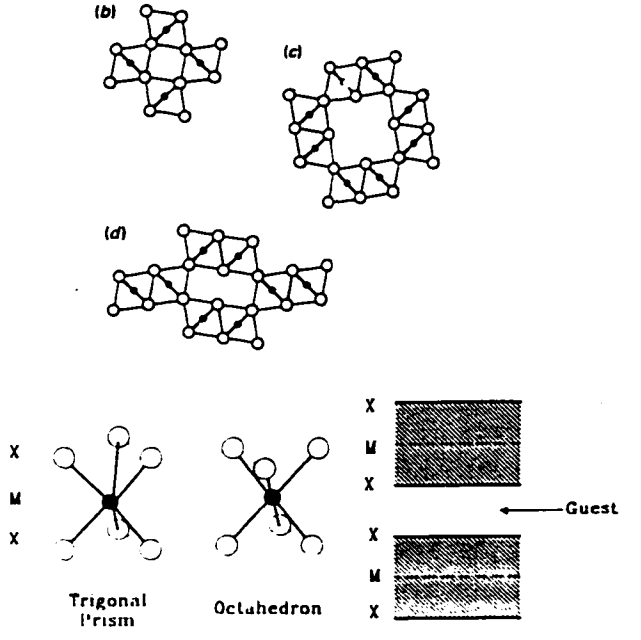

Figure 6
2D systems a)tunnel structures (view from top): i) 1X1 tunnels (TiO_2); ii) 2X2 tunnels as in hollandite ($BaMn_8O_{16}$); iii) 2X1 tunnels as in ramsdellite (MnO_2). b) layered structures: X-M-X type sandwiches and octahedra types

A given compound is sometimes found with different stacking sequences, or *polytypes*. In these there can be differences in the coordination or/and the stacking sequences [19]. Intercalation can induce transition between polytypes. An example of this is the previously mentioned Li_xMoS_2. This structure goes from the hexagonal 2H form, AbA BaB to the 1Tform, AbC AbC. Intercalation

Reproduced with permission of the copyright owner. Further reproduction prohibited without permission.

can also change the stacking sequence without changing the coordination of the transition metal ion. Li_xZrS_2 displays this behavior. Li causes the layers to shift from 1T, or AbC(b)AbC(b)AbC, to the rhombohedral 3R form, AbC(a)BcA(b)CaB [20]. In the 3R form the Li and Zn ions are farther removed from one another than in the 1T form, so the effect is to reduce the Coulomb repulsion between the Li and Zn ions. In general Li prefers octahedral sites at low concentrations. Sometimes a compromise must be reached when there are not enough octahedral sites available. For example, in VSe_2, there is only one octahedral site per transition metal ion. Beyond $x = 1$, therefore, some of the Li ions must start occupying tetrahedral sites. The octahedral sites are squeezed in a plane lying between the tetrahedral site planes, above and below. With the addition of lithium the ions minimize their repulsive energy by moving completely into the tetrahedral sites, thus maximizing their separation. The structural phase transformation is from AbC(b)AbC at x=1 to AbC(a,c)AbC at x=2 [21].

The layered oxides LiNiO2 and LiCoO2 also have the 3R form AbC(a)BcA(b)CaB. In this structure the oxygen lattice considered alone has cubic close packing ABCABC. As a result, both of these compounds are closely related to cubic compounds. A simple way of picturing their structure is to start from cubic NiO and CoO, which have AbCaBcAbCaB structure, and replace every second layer of Ni or Co by Li. In the case of Ni this replacement may be incomplete, and the

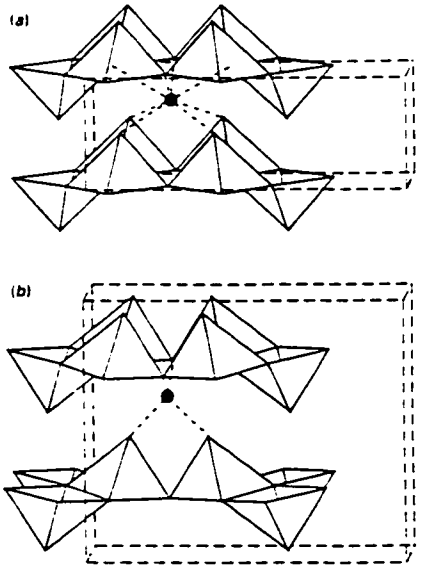

Figure 7 Partial structures of a) V_2O_5 and b) LiV_2O_5. The solid circle is a possible (a) and actual (b) site for Li. The unit cell in b is twice as large, because of the layer displacement.

Reproduced with permission of the copyright owner. Further reproduction prohibited without permission.

lithium layers may contain residual Ni [22].

More complicated layered structures are also possible. Examples of these include V_2O_5 [23] which cannot be described by the ABC notation. One must use coordination polyhedra to represent these structures. In that sense they are quasi-three dimensional. Fig. 7 shows a comparison between the structures of V_2O_5 and beta-LiV_2O_5. Each V is surrounded by a pyramid of five oxygen. Introducing Li causes the layers to shift, producing smaller sites for Li [24].

1.3.2 Three-dimensional Structures

Several three-dimensional structures (both the site and the host compound lattice require a 3D description) are common among some potentially important intercalation compounds. The following is a very general classification of these.

1.3.2.1 Chevrel type structure

This structure is exhibited in a compound like Mo_6Se_8. In the latter, the Se atoms are at the corners and the Mo at the center of a cube face. The individual cubes are arranged in a lattice that is almost cubic, except for a slight rotation of the cubes which allows Mo in one cube to bond with Se in the adjacent one (Fig. 8). This arrangement allows large guests to occupy the cubic sites of the

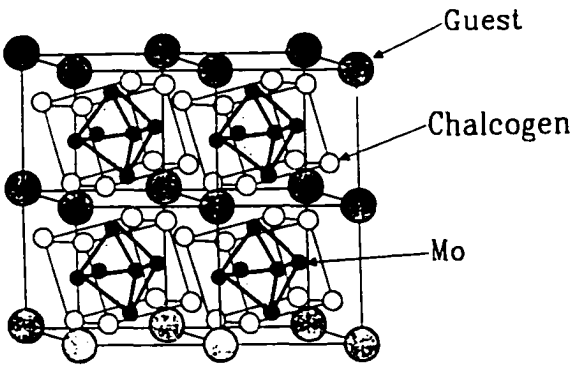

Figure 8 Structure of a Chevrel type compound like Mo_6Se_8.

Reproduced with permission of the copyright owner. Further reproduction prohibited without permission.

envelope lattice if the hosts are small. The electronic structure of these compounds is similar to the one in Fig. 5,except that there are different number of states in the upper and lower bands. The Mo-Mo type bonds split the *d* states into two bands [25]. The lower band contains 24 states per Mo_6Se_8 cluster, because there are 12 Mo-Mo bonds in each cluster (the 12 edges of the Mo_6 octahedron). Each Mo contributes six electrons to the bands, for a total of 36, but of those, 16 go to occupy the Se *p* bands, leaving 20 in the lower *d* band.

1.3.2.2. Perovskite type structures

In perovskites of formula ABO_3, the octahedra BO_3 lie on a cubic lattice, and are joined at the corners. Between these octahedra are larger sites for the A atoms. In ReO_3, the A atoms are missing, so guests can be added to the A positions. Because adjacent octahedra are joined only by one oxygen, they can rotate relative to one another, changing the shape of the A site. In Li_2ReO_3, the rotation splits the large A sites into smaller sites more suitable for Li ions [26]. Other compounds with a perovskite type structure are bronzes of WO_3.

1.3.2.3. ReO_3 type structures

The structure of ReO_3 can often be used as a starting point for describing other structures. For example, the layered structure of V_2O_5 can be derived from that of ReO_3 by removing planes of oxygen and then shearing the structure. The structure of the three dimensional host V_6O_{13} is derived from that of V_2O_5 by removal of a second set of oxygen planes, and then a second shear [27].

Reproduced with permission of the copyright owner. Further reproduction prohibited without permission.

1.3.2.4. Spinel type structures

Spinels are cubic compounds, but the structure can be described as layers of close-packed oxygen. The sites available for both the transition metals and guests are octahedral and tetrahedral, as in Fig. 3a. Unlike the layered compounds in Fig. 6b, however, where every second metal layer is empty, the host metal atoms host occupy octahedral or tetrahedral sites in every layer.

1.3.3 Thermodynamics of the Intercalation Process

1.3.3.1 Chemical Potential

The study of the thermodynamics of the intercalation process allows the comparison of theoretical models with macroscopic measurable quantities. The goal as with any physical model is to minimize the number of free parameters by deriving each quantity from basic principles. An important question is to what extent one can apply thermodynamical principles to the description of the insertion process, since the resulting compound is often metastable at high temperatures. The change of composition is assumed to occur much slower that the relaxation time associated with the insertion process. The most important aspect of insertion is that the concentration of guest can change. The change in the Gibbs free energy with respect to n, where n is the number of intercalated host is by definition the chemical potential μ

Reproduced with permission of the copyright owner. Further reproduction prohibited without permission.

$$\mu = \partial G / \partial n \tag{4}$$

The chemical potential, in turn, is equal to the voltage between the electrodes in a cell. In a cell where the anode is Li metal with chemical potential μ_0, the work in carrying ze electrons through an external circuit will be equal to the work per intercalated ion ($z = 1$), namely

$$W = -z\, e\, E \tag{5}$$

The work must be equal to the change in the free energy

$$-z\, e\, E = \mu - \mu_0 \tag{6}$$

where μ is the chemical potential of Li in the host. If the voltage between the electrodes is measured a function of x (Li content) one can plot the chemical potential as it changes with x. The zero on the voltage scale will denote the limit of intercalation. The deposit of Li will start to accumulate on the surface of the electrode when that limit is reached. The plot of $V(x)$ usually reveals important information about the thermodynamics of the electrochemical system. A more sensitive quantity which is used in this type of analysis is the derivative $-\partial x\, \partial V$ (the negative sign needed because V decreases with x). In particular, first and second-order transitions appear as peaks in this function, since the voltage remains constant as insertion proceeds. The latter changes the relative size of domain structures corresponding to different phases of the intercalated compound; one with smaller and one with larger values of x in a first-order transition. As a rule first-order phase transitions exhibit a *hysteresis*, i.e. the voltage plateaux is higher on charging compared to discharging. In higher order (continuous) phase transitions there is no phase coexistence; instead $-\partial x\, \partial V$ diverges at a single compositions; this according to Ref.28 is analogous to the divergences in specific heat or magnetic susceptibility.

Reproduced with permission of the copyright owner. Further reproduction prohibited without permission.

1.3.3.2. Partial Entropy

The chemical potential may be written as the sum of two contributions, one from the enthalpy and another from the entropy

$$\mu = \partial G / \partial n = \partial H / \partial n - T \partial S / \partial n \quad , \tag{7}$$

where T is the absolute temperature. Using Maxwell's relations and choosing T and n as the thermodynamical coordinates, one can write

$$(\partial \mu / \partial T)_{n = const} = (\partial S / \partial n)_{T = const} \tag{8}$$

Since V is proportional to μ (Eq.), $\partial S/\partial n$ can be measured from changes of $V(x)$ with temperature. The problem with this type of measurement arises from unwanted thermoelectric voltages generated in the cells as the temperature is cycled for different values of x [29]. An alternate method is to measure the heat that flows into an electrochemical cell as it is charged/discharged at *constant temperature*. A calorimeter is needed to measure the heat flow during the experiment. This is related to the internal energy of the intercalation compound and the work W_k done on the cell. Dahn *et al.* [30] proposed the following relationship:

$$\begin{aligned} dQ / dt &= dV / dt - dW_k / dt \\ &= T[(\partial S / \partial n) - (\partial S / \partial n)_0] I / e - I\eta \end{aligned} \tag{9}$$

where t is time and I is current. The subscript 0 refers to the Li anode, and η is the difference between the measured and equilibrium voltage (overvoltage). By measuring dQ/dt one can, therefore, obtain the difference between $\partial S/\partial x$ for the two electrodes, if η is small enough.

Reproduced with permission of the copyright owner. Further reproduction prohibited without permission.

1.3.3.3 Lattice-gas models of intercalated compounds

The above discussion becomes relevant when macroscopic quantities measured in experiment are being compared to theoretical predictions based on lattice-occupancy models, also known as lattice gas models. Such models are analogous to the Ising model for a spin system, for example. In applying a lattice gas model, one must make certain assumptions about the contributions of the electrons and ions of the intercalated metal. A common simplifying assumption is that the chemical potential consists of an ionic and electronic term, the latter being equal to the Fermi energy and constant during the intercalation process.

$$\mu = \mu_i + \mu_e \tag{10}$$

One can solve different lattice gas models the energy and entropy are determined from the distribution of ions over the available guest sites. In the simple but very important case of non-interaction ions being distributed over equivalent sites at random, the entropy is

$$S = -N_s k[x \log x + (1 - x)\log(1 - x)] \tag{11}$$

where N_s is the number of available sites, x the fraction of those occupied, and k Boltzmann's constant.

The partial entropy that can be compared to experiment is then simply

$$\partial S / \partial n = k \log[x / (1 - x)]. \tag{12}$$

Reproduced with permission of the copyright owner. Further reproduction prohibited without permission.

Denoting the energy required to intercalated one ion into the lattice by ϵ, the chemical potential becomes

$$\mu = kT \log[x/(1-x)] + \varepsilon \tag{13}$$

The last equation ignores the interaction between the ions. The simplest approximation which includes this interaction is one in which the energy of interaction is added in the following way. If U is the total energy of interaction per ion when all the sites are full, then it would cost Ux energy to add an ion when x of the sites are occupied. The chemical potential then becomes:

$$\mu = kT \log[x/(1-x)] + \varepsilon + Ux \tag{14}$$

This is called the mean-field expression, since each ion is subjected to the mean field of its neighbors. This procedure assumes than even though the ions interact, they still fill up the lattice at random; i.e. there is no correlation between the type of site lattice and the entropy. The latter only depends on the number of available sites. As a function of x, the mean field expression generates s-shaped curves (Fig. 9). The electronic contribution to the entropy is also neglected.

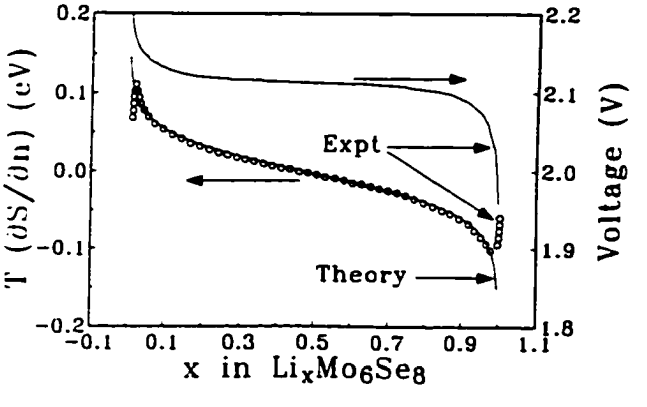

Figure 9 Voltage and partial site entropy in $Li_xMo_6Se_x$ (from Dahn *et al.*).

Reproduced with permission of the copyright owner. Further reproduction prohibited without permission.

1.3.3.4 Electron Entropy

In *metallic* hosts the electronic contribution to the partial entropy is be assumed to be small based on the following argument. Electrons added by intercalation do not have a choice of empty states in a band, but only those within kT of the Fermi energy. According to Kittel [31] the change in entropy with n_e number of electrons, $\partial S / \partial n_e$, is of the order kT / T_F, not order k like Eq. 12 for the intercalating ions. Therefore, under typical conditions, the electronic contribution is much smaller. In other compounds the situation is much more complicated. For example, in a typical transition-metal oxide host, the added electrons are to a large degree *localized* on the transition metal ion. Such a system is considered to be a mixture of transition metal valances. The entropy, in that case, might be considered to be a result of the random distribution of two valence states over the lattice of the transition metal ions, i.e., of the same form as in Eq. 12. The problem with this assumption is that very rarely are these valences distributed randomly. The coulombic interaction between host ions and guest, i.e. V^{+3}, V^{+4} and Li^{+}, in $Li_xV_6O_{13}$, is large and moves the distribution away from random. The result is a more complicated and intricate entropy dependence than simple doubling of Eq. 12.

Reproduced with permission of the copyright owner. Further reproduction prohibited without permission.

2. Research Methods

The main investigative tool employed in the research presented in this thesis is synchrotron x-ray absorption spectroscopy. This includes the collection of data (both *in situ* and *ex situ*) followed by near edge x-ray fine structure (NEXAFS) and extended x-ray absorption fine structure (EXAFS) analysis. Other methods, such as electron paramagnetic resonance (EPR) have also been utilized. We devote this chapter to the discussion of the underlying theory behind both EXAFS and NEXAFS along with basic principles of the experimental setup, instrumentation and data analysis that is required in order to extract physical information from the system being studied.

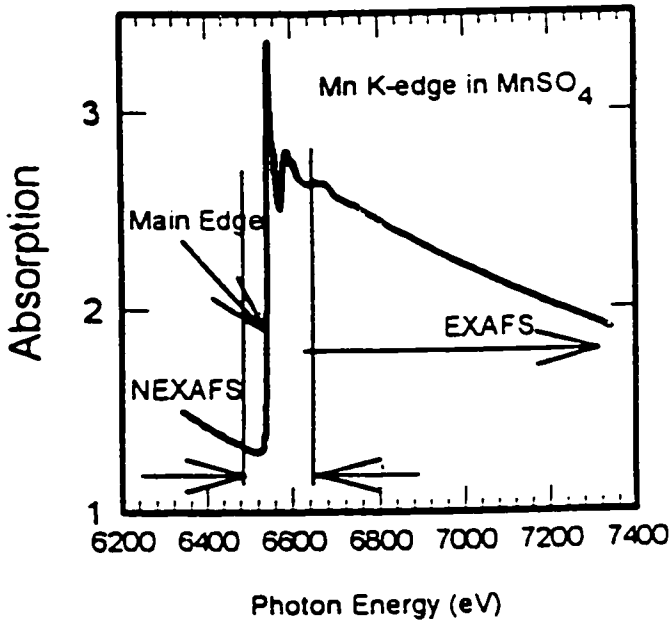

Figure 10 Mn K-edge absorption spectrum in $MnSO_4$ showing the different regions.

2.1 EXAFS

Although both NEXAFS and EXAFS are part of the same continuous x-ray absorption spectrum (XAS) (Fig.10) of each material with respect to photon energy, they refer to different regions in it and are due to different types of electronic transitions within the absorbing atoms. The EXAFS region refers to the oscillations in the absorption spectrum as a function of photon energy from about 40 eV to 1000 eV above the main absorption edge. A short-range single scattering model for this effect has been well established [32]. The free core-photoelectron wave vector, k, is given by

Reproduced with permission of the copyright owner. Further reproduction prohibited without permission.

$$k=\sqrt{\frac{2m}{\hbar^2}(E-E_0)} \tag{15}$$

where E is the x-ray photon energy, E_0 the threshold energy for the particular edge measured. Note that this origin does not coincide with the edge of the conduction band but falls in the occupied valence levels. The minimum wavevector that can be measured, therefore, is always finite, i.e. k_{min} is typically around 2Å^{-1}. In the presence of neighboring atoms the photoelectron will experience backscattering and the absorption rate will be modulated due to the interference of the initial and final electron state (outgoing and incoming photoelectron wave). The experimentally measured absorption rate, $\mu(E)$ as a function of photoelectron energy, can be normalized to the atomic-like backrground edge absorption, $\mu_0(E)$,

$$\chi(E)=\frac{\mu(E)-\mu_0(E)}{\mu_0(E)} \tag{16}$$

where $\mu_0(E)$ is considered to be the embedded atom absorption, i.e. the absorption in the cluster potential of neighboring atoms, neglecting the backscattering interference at the core electron. This absorption is, of course, impossible to measure, therefore it has to be modeled numerically. In order to measure physical parameters on the basis of Eq. 16, one must have some kind of a theoretical model, preferably an *ab-initio* one for this quantity. The single scattering plane-wave approximation of (13) in the case of the excitation of an s state photoelectron wave back scattered from N_j neighbors at r_j distances from the central atom is

$$\chi(k)=\sum_j \frac{N_j}{kr_j^2} f_j(k,\pi)\sin[2kr_j+\psi_j(k)]e^{-2\sigma_j^2 k^2} e^{-\frac{2r_j}{\lambda_j(k)}} \tag{17}$$

Reproduced with permission of the copyright owner. Further reproduction prohibited without permission.

where $\chi(k)$ is the normalized EXAFS, f_j is the backscattering amplitude, and $\psi_j(k)$ is the total phase function. The first exponential factor, called the Debye-Waller term, accounts for losses due to thermal vibrations of the scattering atoms, while the second one is a damping term due to inelastic losses. More precisely, σ_j^2 is the mean square average of the displacement about the ideal atomic position, and λ_j can be interpreted as the electron mean free path. It is the limited range of the photoelectrons in the energy region 40-1000 eV imposed by this term that allows a short-range order description of EXAFS even in crystalline materials. Equation (17) contains all the physical parameters that can be extracted from the data. The local atomic structure information available from EXAFS then is the coordination number, N_j, the interatomic distance, r_j, and the Debye-Waller factor. The amplitude function, f_j, only on the type of backscattering atom. The phase function, $\psi_j(k)$, however contains contributions from both the absorber and backscatterer

$$\phi_{ij}(k)=\phi_i(k)-\phi_j(k)-l\pi \tag{18}$$

where l =1 for K and L_1 edges. Here $\phi_i'(k) = 2\delta_l$ is the l phase shift of the absorber and $\phi_j(k) = \theta$ is the phase of the backscattering amplitude.

By comparing the EXAFS spectrum of an unknown compound to a model compound, one can, in principle, determine the coordination number N_j of the absorber, the bonding length between absorber and neighboring atoms, and the Debye-Waller factor σ_j^2 which accounts for thermal vibrations and static disorder of the central atom. Unlike x-ray diffraction which probes long-range ordered structure, the EXAFS technique probes the local environment of the absorbing atom. Therefore, this technique can be applied to the study of the microstructure of disordered materials, such as amorphous transition metal oxides.

Reproduced with permission of the copyright owner. Further reproduction prohibited without permission.

2.1.1 Amplitude Functions and Phase Shifts in EXAFS

Equations 16 and 17 show that each EXAFS wave contains two sets of highly correlated variables: $\{f_j, \sigma_j, \lambda_j, N\}$ and $\{\psi_j(k), E_o, r\}$. Significant correlations can occur within and between these two sets of variables as well as between different scattering terms. To determine the coordination number, N_j, and the Debye-Waller factor, σ_j, the amplitude function, f_j, must be known reasonably well. To determine the interatomic distance r, the phase shift function, $\psi_j(k)$, must be known accurately.

While both f_j and $\psi_j(k)$ can be determined empirically from model compounds, they can also be calculated from first principles. Advances in the theory along with increase in speed to cost ratio of computing power have made the second method the predominant one.

2.1.2 Static Disorder and Thermal Vibrations

The Debye-Waller factor, σ_j, plays an important role in EXAFS spectroscopy. It contains structural and chemical information which is otherwise difficult to obtain, yet it comes as a bonus in the EXAFS determination of interatomic distances. In general, the Debye-Waller factor includes both static disorder and thermal vibrations contributions, σ_{stat} and σ_{vib}. They are uncorrelated and both can be derived from the pair distribution function $g(r)$ through the following equation

$$\chi(k) = \frac{F(k)}{k} \int_0^\infty g(r) e^{-2r\lambda(k)} \frac{\sin(2kr + \phi(K))}{r^2} dr \qquad (19)$$

Reproduced with permission of the copyright owner. Further reproduction prohibited without permission.

In general, $g(r)$ depends on the interatomic potential. For σ_{vib} in particular, $g(r)$ depends on the vibrational frequency and the absolute temperature.

Assuming that the static disorder is small with a symmetric pair distribution function and that the thermal disorder is due to harmonic vibrations, we may write

$$\sigma^2 = (\sigma^2)_{stat} + (\sigma^2)_{vib} \tag{20}$$

The term σ_{stat} is related to the symmetric Gaussian pair distribution function

$$g(r) = \frac{1}{\sqrt{2\pi}\sigma_{stat}} e^{-(r-r_0)^2/2\sigma_{stat}^2} \tag{21}$$

where r-r_0 is the deviation from the mean distance r_0.

Assuming a harmonic motion for a diatomic system, the vibrational contribution to the Debye-Waller factor in the Debye approximation is given by [33], [34]

$$\sigma_{vib}^2 = \frac{\hbar}{2M_r}\int \rho(\omega)\coth\left(\frac{\hbar\omega}{2k_BT}\right)\frac{d\omega}{\omega}; \quad M_r = \frac{M_iM_j}{M_i+M_j} \tag{22}$$

where

$$\rho(\omega) = \frac{3\omega^2}{\omega_D^3}\left(1 - \frac{\sin(\omega R_j/v)}{\omega R_j/v}\right); \tag{23}$$

and

$$\omega_D = \frac{k_B\Theta_D}{\hbar} \tag{24}$$

Reproduced with permission of the copyright owner. Further reproduction prohibited without permission.

and is derived from the Debye temperature Θ_D, $\nu = \omega_D / k_D$, where $k_D = (6\pi^2 N/V)^{1/3}$ and V is the crystal volume.

In principle, these two components (σ_{stat}, σ_{vib}) of the Debye-Waller factor can only be separated by a temperature-dependent study of $\sigma(T)$. However, if σ_{vib} can be estimated from vibrational spectroscopies or if σ_{stat} is known from other studies, the other term can be calculated from the experimentally determined σ.

Fourier Transform Amplitude Function

The Fourier transform of both sides of Eq. 17, after slight rearrangement will yield a function of r which may be written as:

$$F(r) = 1/2\pi \int_{k_{min}}^{k_{max}} \frac{W(k) k^n \chi(k) \exp[-i(2kr + \psi_i)]}{f(k) \exp(-2k^2\sigma^2)} \qquad (25)$$

where $W(k)$ is a suitable window function, k^n is a weighting factor which can roughly compensate for the quadratic dependence of $f(k)$ when $n = 3$. The amplitude of this function (FTA) is closely related to the true radial distribution function of the absorber (RDF), and for the purposes of qualitative assessment of the local structure may be used as blueprint for the latter. The peaks in the FTA, although phase shifted from the true atomic positions [ ] correspond to different shells of atomic neighbors. While this function is a useful guide for assessing local structure, it contains various artifacts which have to be carefully taken into account during the analysis phase of the x-ray absorption experiment. The most important are:

1. There is always a residual structure coming from the finite range ($\Delta k = k_{max} - k_{min}$) of the

Reproduced with permission of the copyright owner. Further reproduction prohibited without permission.

data and to a lesser extent from the concrete form of the window function $W(k)$.

2. $F(r)$ can only be phase-shift corrected for a particular near-neighbors peak.

3. The simple single-scattering plane-wave approximation (PWA) from which Eq. 14 is derived introduces inaccuracies. The more accurate theories of this effect necessarily employ more realistic spherical, rather than plane-wave approximations to the final state electron wave function ψ_f. The current code implementation of one of these theoretical models (FEFF) will be discussed in the data analysis section of this chapter.

Reproduced with permission of the copyright owner. Further reproduction prohibited without permission.

2.2 NEXAFS

NEXAFS refers to the region in the spectrum close to the absorption edge E_o (from about 10 eV below to as much as 50 eV above the edge), as shown if Fig. 3. The absorption, in the dipole approximation, is proportional to the transition probability between the initial (core) ψ_i and final states ψ_f

$$\mu(E)=(4\pi^2/\Omega)\alpha h\nu\sum_f <\psi_i|\hat{e}\cdot r|\psi_f>^2\delta(h\nu-E_f+E_i) \tag{26}$$

where Ω is the unit cell volume, $\alpha = e^2 / \hbar c$ and e is the polarization vector of the incident photon. The NEXAFS regime differs from that of the EXAFS with respect to the types of unoccupied final states ψ_f. These encompass all the unoccupied states from the Fermi level up to the nearly-free photoelectron EXAFS limit. In transition metals, such as the ones dealt with in this thesis, the NEXAFS states include the unoccupied part of the narrow *d* bands, just above the Fermi level, as well as the less tightly bound *s* and *p* bands. Unlike the EXAFS regime, a single scattering picture is not sufficient to describe the modulation of the absorption coefficient with energy, due to strong multiple scattering of the electron from neighboring atoms. NEXAFS is thus inherently sensitive to the chemical environment and local symmetry of the absorbing ion. Two approaches are possible for determining ψ_f. The first one involves scattering calculations and the second - band structure calculations. The former is applicable where ψ_f is a solution to the excited atom potential. This solution is improved to include single backscattering from neighboring atoms, spacial variations of the scattered wavelets and multiple scattering effects at low energies. Band structure formalism, on

Reproduced with permission of the copyright owner. Further reproduction prohibited without permission.

the other hand, uses a periodic potential and includes multiple scattering to infinite order. Even though full calculations of this spectral region, based on either multiple scattering theory [35], band structure formalism, or a combination of the two [36], still lack sufficient accuracy for most materials, important chemical information can still be extracted by observing positions, intensities and shapes of distinct features. The following sections will focus on these main features of the NEXAFS.

2.2.1 Pre-edge Feature

A fine structure in the NEXAFS is sometimes observed below the main edge. This is usually referred to as the *pre-edge*. Relative changes in the intensity of the pre-edge peak (Fig. 11), corresponding to the dipole forbidden 1*s*-n*d* transitions in transition metals, give information about the degree of deviation from local octahedral symmetry and the degree of mixing of the *d*-type orbitals of the cation with the *p*-type orbitals of the anion.

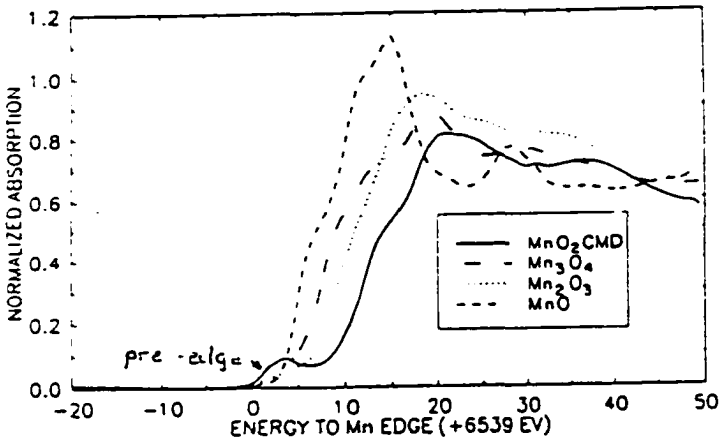

Figure 11 Comparison of near-edge Mn XAS (NEXAFS)for CMD MnO2 with those for Mn_2O_3, Mn_3O_4 and MnO (From B.E. Conway, D. Qu and J. McBreen)

Reproduced with permission of the copyright owner. Further reproduction prohibited without permission.

2.2.2 White Line

The White Line (WL) peak (Fig. 11) in Ar gas is due to the first of a Rydberg-type series of $1s \rightarrow np$ transitions, where $n > 3$, which converge in the absorption limit of $1s \rightarrow \infty$. These are not transitions to the continuum, therefore corresponding to photoelectron behavior, but to bound states. Usually only the first several transition peaks are discernable, of which the WL is the most prominent. The reason is that each peak is broadened by the Auger-effect decay of the corresponding discrete lines. There is also the inherent broadening due to the finite width Γ_i of the inner K level. In the case of Ar gas, this is 0.58eV. The WL and the following called by Parratt *bound-ejected-electron* excitation states [37] mask the true onset of photoelectron transitions which is characterized by an arctangent shape. Parratt devised a simple method of fitting the absorption edge, when the latter has the WL as part of the structure. The arctangent curve with the corresponding Γ_i is drawn at the Rydberg series limit to merge with the observed continuous curve. The resolved peaks preceding the arctangent are fitted as Lorentzian emission lines with the same Γ_i half-width. The remaining lines are drawn at the Rydberg positions, with adjusted amplitudes to fit the overall curve when added to the arctangent curve. The inflection point of the fitted arctangent

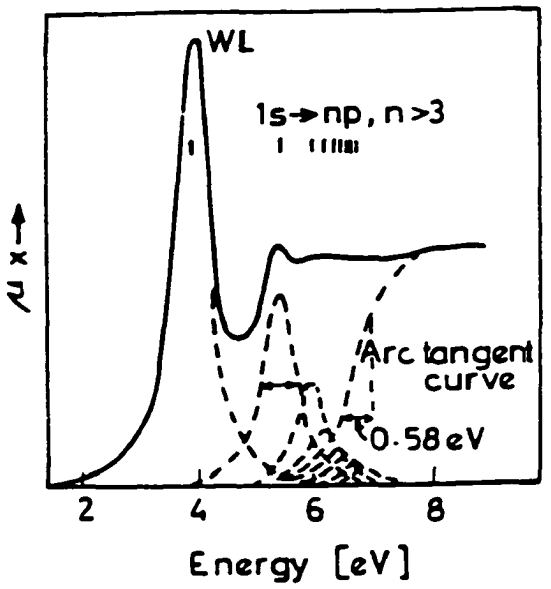

Figure 12 WL decomposition for gaseous Ar. From B.K. Agarwal (Ref. 64)

Reproduced with permission of the copyright owner. Further reproduction prohibited without permission.

curve is the true main edge position.

In solids the WL can arise if there are unoccupied states of the required symmetry with a high density of states at the absorption edge [38]. The well known cases are the $L_{II,III}$ edges ($2p \rightarrow nd$) of transition elements where there is a high density of empty d states.

2.2.3 Main Absorption Edge and Chemical Edge Shift

The theory of the main absorption edge as applied to both metals and semiconductors was first given by Richmyer *et al.* [39]. The main idea is that a series of transitions from inner core states to bound resonance states, also called optical levels, gives rise to discontinuity which is know as the *main edge* or edge jump. This can be modeled with an arctangent curve, the inflection point of which can be identified with the energy position of the absorption edge. The width of inner core levels completely determines the with of the edge itself. It is assumed that the transitions to states beyond the Fermi levels involve a wide band of allowed states.

The interpretation of the main edge becomes complicated when one analyses transition metals with incomplete d shells. The reason for this is the s-p-d hybridization that occurs between the orbitals. It becomes convenient the describe the situation in terms of a density of states curve, $N(E)$, which give the number of orbitals for each admissible energy value E:

$$N(E) = N_{occ}(E) + N_{unocc}(E) \tag{27}$$

where N_{occ} (N_{unocc}) denote the density of occupied (unoccupied) states. The absorption rate then

Reproduced with permission of the copyright owner. Further reproduction prohibited without permission.

becomes

$$\tau(E) \propto P_{ab}(E) \cdot N_{unoc}(E) \tag{28}$$

where P is the transition probability.

An important property of x-ray absorption revealed in the early days of this spectroscopy is that chemical bonding affects the position and shape of the main edge. The effect is known as the *chemical shift* of the main edge. The shift of the absorption edge i (i =K, L, M,...) of an element in a compound is measured with respect to the pure element:

$$\Delta E_{chem.} = E_i \text{ (compound)} - E_i \text{ (element)} \tag{29}$$

In general, the shift ΔE_{chem} is positive (towards higher energy) and ranges usually from ~ 1 eV to ~ 15 eV.

Two main factors contribute to this high energy shift: a) the tighter binding of the core level because of the change in effective charge (screening) of the nucleus caused by the partaking of the valence electrons in the chemical-bond formation and b) the appearance of an energy gap when one goes from a metal to a chemical compound (semiconductor or insulator). Various empirical or semi-empirical rules have been given to account for this effect. One, stated by Agarwal and Verma [40]is: *In general, the chemical shift is toward the high-energy side of the metal edge; it increases progressively with increase in the valence of the cation, unless the shift is either suppressed by the covalent character of the bond or enhanced by the formation of metal-metal bonding.*

Ovsyannikova *et al.* [41] give the following empirical formula for calculating the edge shift:

Reproduced with permission of the copyright owner. Further reproduction prohibited without permission.

$$\Delta E_{c.sh.} = const.\ [\ N - (1 - f_i)n\ ] \qquad (30)$$

where N is the valence, f_i is the Pauling ionicity for a crystal, n is the coordination number. Dey and Agarwal [42] suggest another formula:

$$\Delta E_{c.sh.} - \delta E = const.\ N^2 f_i \qquad (31)$$

where δE is the promotion energy required to promote an electronic ($s \rightarrow p$) transition in the atom, in order to enable it to display the required oxidation number. Different studies indicate that in many systems $\Delta E_{c.sh.} \propto q$ (effective charge). For example, Chetal and Mahto have measured the edge shift in various Co compounds in which Co has a range of different formal oxidation states [43]. The compounds exhibit widely different crystal structures and contain different types of bonding and various types of ligands. They arrive at a quadratic formula for the fit to experimental data:

$$\Delta E_{c.sh.} = Aq - Bq^2 \qquad (32)$$

where q is the effective charge calculated by using Suchet's method,

$$q = n\ [\ 1 - 0.01185\ (\ z\ r' - z'\ r\ )\ ]\ , \qquad (33)$$

where z (z') and r (r') represent the total number of electrons and the ionic radius of the cation (anion) respectively, and n is the valency (formal oxidation number) of the cation in the system. The leading term in Eq. 32 is obviously the linear one, as can be seen from the fit to the data (Fig. 12).

Reproduced with permission of the copyright owner. Further reproduction prohibited without permission.

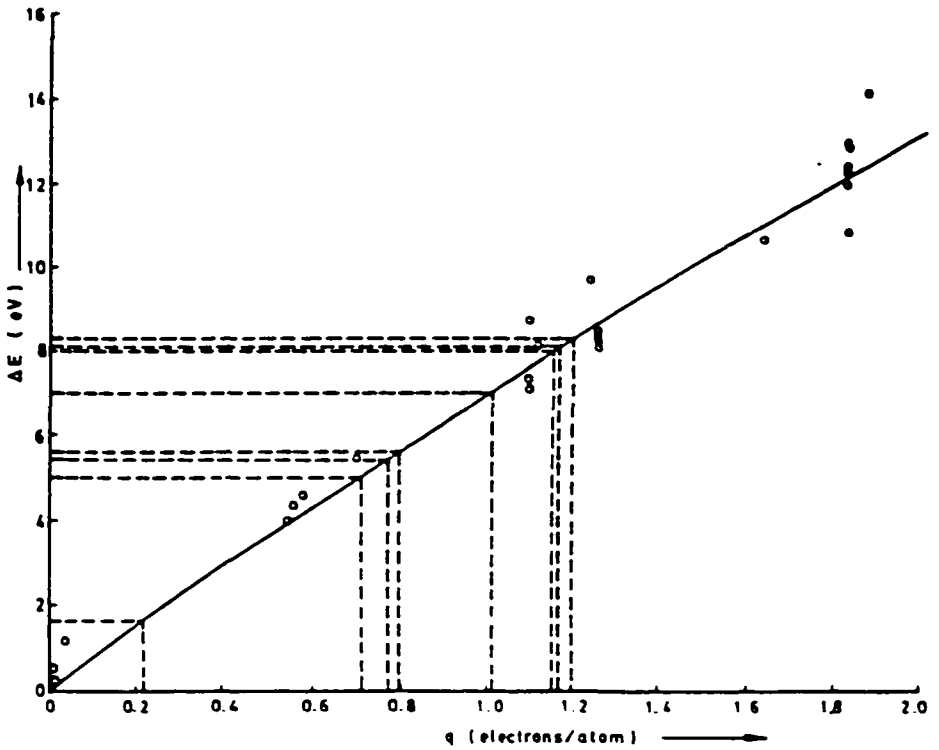

Figure 13 Plot showing the dependence of the chemical shift, ΔE_{sh}, on the effective charge, q, for some Co compounds (From Ref. 43)

Reproduced with permission of the copyright owner. Further reproduction prohibited without permission.

3. Experimental Techniques

X-ray absorption spectroscopy utilizes a variety of different experimental techniques. Fig. 14 illustrates these schematically. In the transmission geometry that detects the primary process, the whole X-ray absorption is measured. However, the cross section of the element of interest might only be a small fraction of this. A particular partial cross section is more prominent in the excitation spectrum of a secondary process such as x-ray fluorescence or Auger emission. In particular, where photoelectron detection is concerned, the average escape depth of electrons (which is typically 500Å) adds considerable surface specificity to this technique compared to the much longer X-ray attenuation length of several microns which governs X-ray detection.

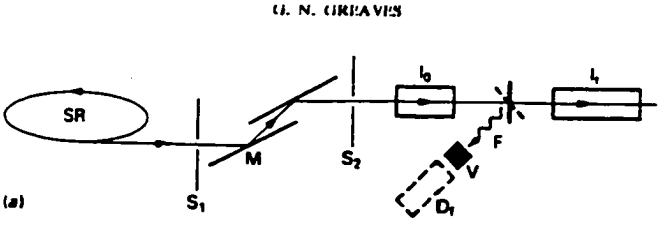

Figure 14
Experimental arrangements for XAS studies. SR: synchrotron radiation source. S1 and S2 vertical slits. M: two crystal monochrometer. V: soler slits. I0, It: ion chambers for transmission measurement. DF: scintillation counter or solid state detector for fluorescence measurement

3.1 Transmission

The standard arrangement used at synchrotron sources for transmission XAS is shown in Fig. 14. Monochromatic radiation with a band pass at least as small as ΔE_{tau} (Eq.) is required and this

Reproduced with permission of the copyright owner. Further reproduction prohibited without permission.

is readily obtained using two bounce crystal monochromators. Silicon is used for X-ray energies down to a few keV. At soft X-ray energies, InSb, Ge or KAP are preferable [44]. Total X-ray absorption, α, is obtained from the ratio of transmitted (I_t) to incident (I_0) beam intensity:

$$I_t = I_0 \exp(-\alpha t) \tag{36}$$

where t is the sample thickness and signal-to-noise ratio is maximized when

$$\alpha t = 2.6. \tag{37}$$

The optimum thickness of a multicomponent sample for a transmission measurement depends of course on the average atomic density. For the same absorption edge, a metal powder sample, for example, will need to be about half as thick as a powder oxide one. At the same time the optimum sample thickness for the same material also depends strongly on the energy of the absorption edge of the element being measured. It is convenient to take 4 keV as the division between hard and soft X-rays. At hard X-ray energies running typically from around 4 up to 30 keV, t for an EXAFS measurement will range from 10 to 100μm. For a synchrotron beam measuring a few mm^2 this represents around a mg of active material. Most EXAFS and XANES experiments are made using hard X-rays in an environment of air. The following table gives a demarcation of the type of edge and atomic type which could be measured.

Reproduced with permission of the copyright owner. Further reproduction prohibited without permission.

Energy Range	Edge Type	Elements	Comments
500 eV-4 eV	K L	O→K V→ Sn	Vacuum required. Limited use for multicomponent systems
4 keV-30 keV	K L	K→ Sn Sn →U	Measurements can be made in air. Suitable for most multicomponent systems

Table 1. XAS Energy Ranges

Measurements of elements lighter than oxygen are possible but the separation between edges of different elements is sufficient only for XANES studies. The particular problems of working in the soft X-ray region are considered have to be taken in to account [45]. Note the switch to L-edges for heavy elements. This is due to *electron-hole lifetime broadening* which washes out the fine structure for the corresponding K-edge.

Fabrication of thin-film specimens of amorphous material several mmms thick is straightforward and can be done by depositing onto Al or Be substrates. Thicker specimens are prepared by powdering the sample or pelletizing with an X-ray transparent binder-BN (Boron Nitrite) or graphite. Alternatively, tapes such as kepton or paraffin paper can be used to deposit even layers of the powdered sample. Effective specimen thickness can of course be increased by "doubling over" or inclining at small angles to the incident beam.

The relevant signal, S, in an EXAFS experiment is the normalized fine structure (Eq.16) which is usually a few percentage points of the total X-ray absorption cross section, α_t, of the

Reproduced with permission of the copyright owner. Further reproduction prohibited without permission.

element being measured. This in turn will generally be just a fraction of the total cross section of specimen α. If the concentration of the element in question is c_i

$$S \sim c_i \alpha \chi_i \tag{38}$$

The photon limited noise, N, depends on the geometry employed. For transmission through a sample of optimum thickness

$$N \sim \frac{2\alpha}{\sqrt{I_0}} \tag{39}$$

giving a signal-to-noise ratio of

$$\frac{S}{N} \sim \frac{\chi_i}{2} \frac{c_i \alpha_i}{\alpha} \sqrt{I_0} \tag{40}$$

This clearly falls away linearly with concentration. A value of around 50 is needed for full EXAFS analysis and so for 10^{10} photons per experimental point, Eq. 40 gives a lower limit for c_i of a few percent if the transmission mode is used.

A. FLUORESCENCE

Returning to Fig. 14, characteristic X-ray emission is best collected in a synchrotron experiment at right angles to the beam, where polarization effects minimize the Compton scattering contribution to the background. Raleigh scattering is generally reduced using X-ray filters or an energy discriminating detector. For a dilute system, the characteristic absorption α_i is related to the fluorescence signal I_f by the following relation

Reproduced with permission of the copyright owner. Further reproduction prohibited without permission.

$$I_F \sim I_0 \varepsilon \frac{c_i \alpha_i}{2\alpha} \tag{41}$$

Eq. 41 assumes the specimen is opaque (i.e. $\alpha t \gg 1$). This clearly removes the necessity to fabricate samples with an optimum thickness t. ϵ is the overall efficiency (quantum x solid angle x detector) which can seldom be greater than 5% - the primary limitation being the solid angle. The photon-limited noise

$$N_F \sim 2\sqrt{\alpha \frac{c_i \alpha_i}{\varepsilon I_0}} \tag{42}$$

yields a signal-to-noise ratio for fluorescence detection of XAS

$$\frac{S}{N_F} \sim \frac{\chi_i \varepsilon^{1/2}}{2} \sqrt{\frac{c_i \alpha_i}{\alpha} I_0} \tag{43}$$

Comparing Eq. 40 and Eq. 43 we notice a clear improvement in S/N for the same I_0 of fluorescence compared to transmission as c_i decreases. The two modes have comparable sensitivity as:

$$\frac{c_i \alpha}{\alpha} \sim \varepsilon \tag{44}$$

i.e., for concentrations around 5%. Lower concentrations can be measured using multiple scans and increasing I_0. With present synchrotron sources the minimum concentration is around 0.1% equivalent to an impurity level of around 10^{19} atoms cm^{-3}. This is for an environment of medium atomic number. For heavy or light atom matrices, the minimum concentration may be up to five time greater or less respectively.

For concentrated, thick samples Eq. 43 indicates that the fluorescence signal I_F is non-linear

Reproduced with permission of the copyright owner. Further reproduction prohibited without permission.

in α_i. However, for thin samples $\alpha t \ll 1$ and

$$I_{fl} \sim I_0 \varepsilon c \alpha_i t \tag{45}$$

and the problem of nonlinearity disappears. However, for specimens measured at normal incidence to the X-ray beam, so does the signal. The appropriate geometry for measuring concentrated systems in fluorescence is to employ small angles of incidence. In this case, t is replaced by z, the X-ray penetration depth [46]. Fluorescence techniques are customarily exploited for hard X-ray absorption edges where the X-ray emission efficiency is high. In the soft X-ray range where efficiencies are usually a few percent or less, however, Compton scattering cross sections are almost negligible and energy discrimination of the detector is less important. Accordingly, the overall efficiency of detection, ϵ, can be improved [47].

C. PHOTOYIELD

In the soft X-ray region, XAS is most conveniently measured by detecting photoemmision from the sample. After all, a vacuum environment that which is essential for electron detection is also necessary for soft X-rays because the attenuation in air is so great. At the same time, at low photon energies, Auger emission dominates the relaxation process. Unless a characteristic Auger line is windowed for detection, however, photoyield measures the total absorption coefficient, α i.e.

$$I_{fl} \sim I_0 \varepsilon \alpha L \tag{46}$$

where L is the electron escape depth. This increases from around 100Å at soft X-ray energies, to as

Reproduced with permission of the copyright owner. Further reproduction prohibited without permission.

much as 1000Å in the hard X-ray region. For most transition metal oxides the structure at depths as small as 100Å are usually equivalent to the bulk. However, because only a small fraction of the X-ray attenuation depth is sampled, photoyield is inherently less sensitive than transmission, which also detects the total X-ray cross section (Eq. 36 and Eq. 46). Nevertheless photoyield, particularly at the soft X-ray absorption edges, is simpler to measure and sample fabrication less of a problem. At hard X-ray energies, the photoyield technique can also be advantageous if the samples cannot be prepared as thin films or powders. A vacuum environment is not necessary if an ion-chamber geometry is employed [48].

Reproduced with permission of the copyright owner. Further reproduction prohibited without permission.

2.3 DATA ANALYSIS

2.3.1. EXAFS ANALYSIS

In order to extract the structural information present in the EXAFS from the experimentally measured absorption spectrum, one must go through a series of data reduction steps illustrated in Fig. 13. There are variations of this general algorithm, although the main steps are present in one form or another in all analysis schemes. The main tools for implementation of the above procedure in this work have been the UWEXAFS [49] software package and the FEFF [50] program. Progress in the field has expressed itself, among other things, in the division of labor that has occurred within the EXAFS community. That along with the ever increasing ease of distributing software, i.e. Web sites, has benefitted x-ray experimentalists and brought a high degree of efficiency to their effort.

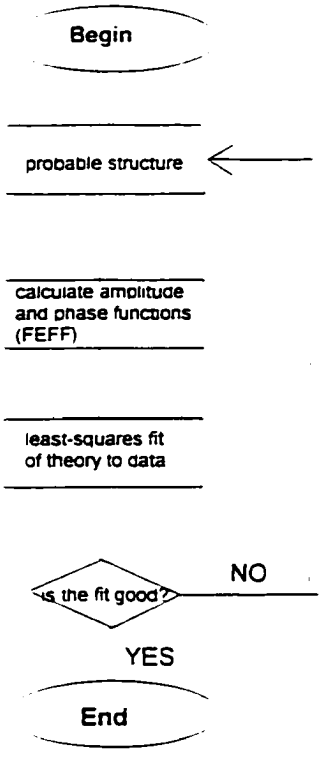

Figure 15
Standard algorithm for EXAFS data reduction.

The UWEXAFS package is one of many software utilities created for the sole purpose of analyzing EXAFS spectra. As of this writing, it still consists of several main routines which are written in ANSI Fortran and could be compiled to run on different platforms. We have used a Pentium PC and the programs were compiled to run on Extended Memory DOS mode. The different

Reproduced with permission of the copyright owner. Further reproduction prohibited without permission.

routines are designed to fulfill different parts of the main procedure (Fig. 15) The following is an outline of the various programs, following the authors' description.

2.3.1.1 ATOMS

This program determines the Cartesian coordinates of the surrounding atoms, relative to a central absorbing atom. These coordinates are, of course, allowed to vary in the subsequent steps of the analysis, but as a starting point or first approximation to the true geometry, they are important. The input for this program is a text file that specifies the crystallographic parameters of the compound. The output is a list of Cartesian coordinates that can be read into Feff in order to calculate the scattering amplitudes and phases in the cluster.

2.3.1.2 AUTOBACK

This program performs the task of interpolating a background (atomic-like embedded) to the raw spectrum, in order to isolate the EXAFS contribution. There is a ongoing discussion on how model the atomic-like background absorption. The correct approximation to this has been frequently discussed in the literature [51], [52]. The traditional approach of modeling the background uses splines, whose nodes are positioned in energy or *k*-space in a more or less intuitive manner. AUTOBACK uses ideas from information theory [53] to argue that the nodes should be equally spaced in k-space by the interval π/R_{min}, and that their fit to the background should be in accordance with the minimization of the low R region as described in Ref. 54.

Reproduced with permission of the copyright owner. Further reproduction prohibited without permission.

2.3.1.3 FEFF

The prevailing method of obtaining structural information has become fitting theoretically calculated spectra to the actual data. The reasons for this are accuracy and reproducibility. Recent advances in the theoretical calculation of the spectra, incorporating multiple scattering theory [55] have, increased the accuracy in determining of both crystalline and amorphous materials. FEFF is the state of the art in numerical simulation of EXAFS-spectra. In its current form, version 6, it can also simulate near-edge absorption, although the accuracy there is much less than the experimental uncertainty of the data. FEFF is really a computer implementation of a sophisticated *ab-intio* multiple scattering, curved wave theory of EXAFS. The following is a brief outline of the main algorithms in the package. FEFF starts out by reading the input (usually written by ATOMS) which gives the first approximation of the absorbing atom and scattering cluster. It then calculates potentials for each of the atoms as if the latter were isolated in space using a relativistic Dirac-Slater Desclaux atom code with a von Barth-Hedin ground state LDA exchange- correlation potential. The scattering potentials are calculated by overlapping the free atom densities within the muffin-tin approximation and including the Hedin-Lundqvist/Quinn self energy for excited states. Muffin-tin radii are determined automatically from calculated Norman radii and scattering phase shifts are determined by matching at the muffin tin radius. XAFS spectra are referenced to the threshold Fermi level, which is estimated by electron gas theory at the mean interstitial density. Atomic configurations and core-hole lifetimes are built in, and mean free paths are determined from the imaginary part of the average interstitial potential. Dipole matrix elements are calculated using atomic core and normalized continuum wavefunctions. An absolute atomic scale is obtained by a

Reproduced with permission of the copyright owner. Further reproduction prohibited without permission.

Desclaux-atom calculation of the total energy of the system with and without the core-hole.

The free atomic potentials need as input only the atomic number of the atoms, and, for the absorbing atom, the type of the core-hole being considered. To do the overlapping for unique potentials, the neighboring atoms must be identified, either by position (from a list of the Cartesian coordinates of each atom) or by explicit overlapping instructions. To save time the code calculates the overlapped atom potential for each unique potential only once, using as a sample geometry the first atom in the list with a given potential index. Thus it is essential that the neighborhood of the atom be appropriate.

Another stage of the calculation of the simulated spectrum is the enumeration of paths FEFF will use to calculate the scattering contributions. The code uses a constructive algorithm with several path filters to explore only the significant scattering paths in order of increasing path length, based on the list of atomic coordinates. An degeneracy checker is used to identify equivalent paths (based on similar geometry, path reversal symmetry, and space inversion symmetry). The criteria used in the filtering are based on increasingly accurate estimates of each path's amplitude. The earliest filters, the pathfinder heap and keep filters, are applied as the paths are being created. A plane wave filter based on the plane wave approximation (plus a curved correction for multiple-scattering paths) and accurate to about 30% is applied after the paths have been enumerated and sorted. Finally, an accurate curved wave filter is applied to all remaining paths.

Next for each path the code calculates the effective scattering amplitude ($|F_{eff}|$, from which FEFF gets its name), total scattering phase shift, and other XAFS parameters using the scattering matrix algorithm of Rehr and Albers. Once the scattering phase shifts and the paths are determined, no other input is necessary for this calculation.

Reproduced with permission of the copyright owner. Further reproduction prohibited without permission.

Finally, FEFF constructs the XAFS spectrum $\chi(k)$ from one or more paths.

2.3.1.4 FEFFIT

The FEFFIT program performs two major tasks. First, it solves the minimization problem of the square of the residuals, namely

$$\min[\sum_{i} \chi^{e}(R_i) - \chi^{c}(R_i)]^2 \tag{34}$$

where $\chi^c(R_i)$ is the theoretically calculated spectrum and $\chi^e(R_i)$ is the experimentally extracted one, and in the process determines the *best-fit values* of physical variables of the model. The spectra can be transformed into R-space, denoted by the independent variable. This gives an added advantage of comparing the fit of the peak structure of the FTA to the experimental data. Second, FEFFIT gives a reasonable estimate of the *uncertainties* in the best-fit values. The actual fitting is done using the standard Marquardt-Levenberg algorithm. The input file allows a path- based approach, characteristic of the FEFF algorithm to be incorporated in the analysis of the fit. The model calculation is given (in k-space) by the equation

$$\chi_{model}(k) = \sum_{Paths} \chi_{path}(k, Amp(k), Phase(k), PathParameters) \tag{35}$$

where *Amp* and *Phase* are the previously calculated FEFF functions for this structural model, and *Path Parameters* are variables which are path specific. One is encouraged to use this in constructing

Reproduced with permission of the copyright owner. Further reproduction prohibited without permission.

functional dependencies which correspond to more interesting physical quatities such as anharmonicity parameters, lattice expansion parameters, etc. Equation 35, in its explicit version, retains the same form as the basic single-scattering approximation (Eq. 17), while at the same time allowing for a path-based multiple scattering model, thus utilizing the accuracy of FEFF ver. 6. The question of the uncertainties is very important when one is comparing small changes in the structural parameters. It is explicitly addressed by FEFFIT. The program treats the uncertainties as due to both random and systematic errors. The random errors are due to the finite statistics of the measurement. Systematic errors incorporate both errors in the measurement, background subtraction theory, and the assumed model.

Reproduced with permission of the copyright owner. Further reproduction prohibited without permission.

2.3.2 NEXAFS ANALYSIS

The rigorous analysis of the NEXAFS region is more complicated than the corresponding EXAFS. The reason is that the multiple scattering contributions which give rise to this structure are difficult calculate. For the purposes of examining *relative* changes in edge position and edge features, such as the ones which occur when a matrix material undergoes lithiation or some other gradual chemical change, other methods are easier to apply.

The standard analysis of the near-edge region requires the normalization of the data with respect to the edge jump. This is necessary since the absorption strength is a function of arbitrary parameters such as sample thickness and relative concentration of active material within the sample. The main edge position, E_0, is determined somewhat arbitrarily as the maximum of the first derivative of the data with respect to energy or in some cases as the inflection point. The pre-edge background, which is an extrapolation of a linear or quadratic fit to the data from around -200 eV to -10 eV (assuming $E_0 = 0$) is subtracted from the entire data region. The remaining data from around 10 eV above the edge position to about 200 eV (after the edge) is fitted with a quadratic or cubic polynomial which is extrapolated into the negative energy region. The height of the edge jump is determined as the difference between the values of the pre-edge and post-fit at E_0. The data is then divided by this factor.

When the edge positions are compared between systems in which the absorbing ion has a very different chemical coordination, certain problems arise. Due to the possible appearance of new features which modulate the absorption edge and change its shape, there may be an uncertainty in assigning even an arbitrary E_0, which may be used to measure the edge shift. In those cases some

Reproduced with permission of the copyright owner. Further reproduction prohibited without permission.

authors have found it more consistent to use other rules in determining this parameter. The position of the point which is at one half the maximum height has been used. This usually includes the White Line and is not well justified when the latter is changing dramatically between samples. Also, the half-width position can be employed if the edge jump is fitted with a Lorentzian or Gaussian type cure. These approaches have little theoretical value, but in some cases are essential to furthering the analysis.

The intensity of spectral features such as the pre-edge and WL, discussed in Ch. 2, can be measured as an integrated area over a smooth background which may be fitted by hand or using an interpolative algorithm over a somewhat wider energy region, one which includes the particular feature. A general problem is that of unresolved peaks which may appear as a single one, but in fact signal the onset of a new type of transition.

Reproduced with permission of the copyright owner. Further reproduction prohibited without permission.

3. Systems Studied With XAS. Results and Discussion

3.1 $Li_{1-x}CoO_2$ Battery Cathodes [56]

Near edge x-ray absorption fine structure measurements were performed on lithium deficient cathode materials $Li_{1-x}CoO_2$, where x = 0.1, 0.4 and 0.6. The samples were prepared electrochemically from the stoichiometric parent compound (x = 0.0). The cobalt K-edge x-ray absorption spectrum of the stoichiometric sample is shown in Fig. N. The small pre-edge peak at around 7705 eV is visible.

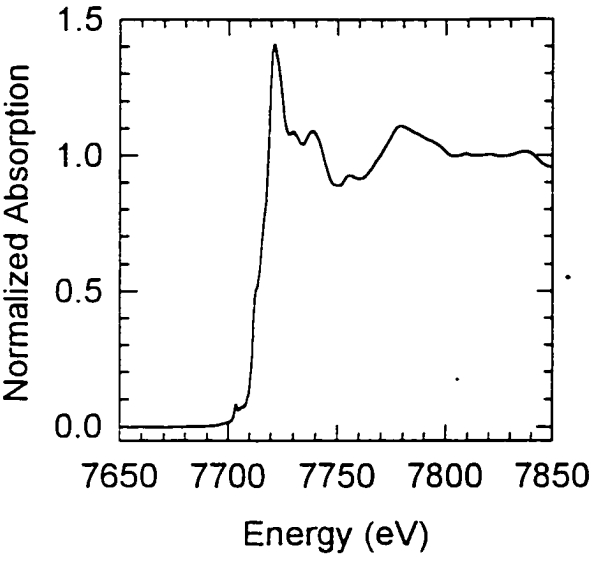

Figure 16 Cobalt K-edge NEXAFS spectra in $Li_{1-x}CoO_2$ series

The main absorption edge exhibits a shoulder and the white line is relatively sharp. The peak values for the latter are given in Table 2. For the three samples with x-values 0.0 (stoichiometric), 0.1 and 0.4, the peak shifts to higher energy with decreasing Li content. This is attributed to the increase in charge on the Co ion due to the removal of compensating electronic charge associated with the

Reproduced with permission of the copyright owner. Further reproduction prohibited without permission.

lithium deficiency. The relatively large shift (almost 2 eV over the entire range) is consistent with the expectation that the compensating electrons originate from the Co ions rather than from the generation of defect oxide species. There is no significant difference between the peak positions for the x = 0 and x = 0.6 materials, which may be due to the actual Li contents of the two samples being closer to each other than the nominal Li contents, and the presence of the structural phase transition in the lowest Li content sample, which can also affect the edge position.

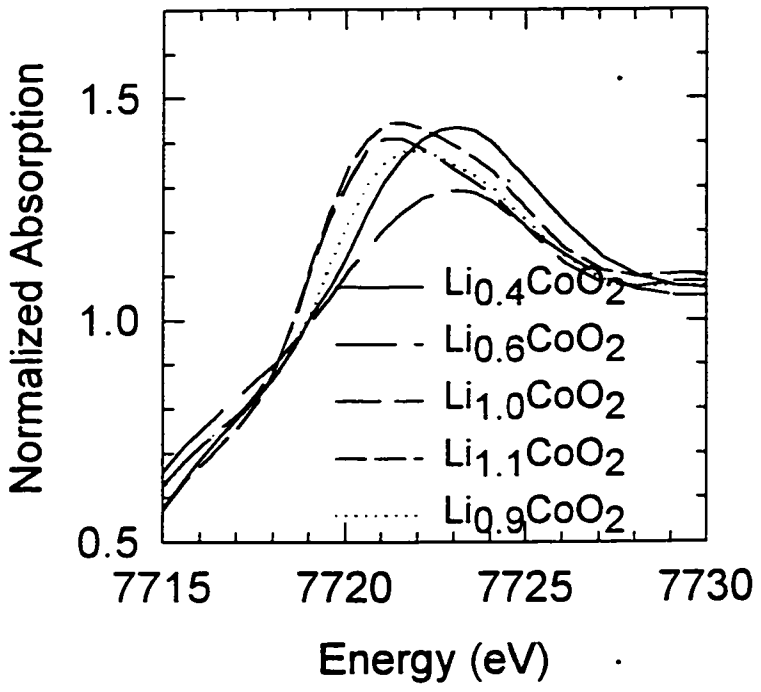

Figure 17 Detailed view of NEXAFS white line for $Li_{1-x}CoO_2$ series.

COMPOUND	WHITE LINE PEAK (eV)
$Li_{0.4}CoO_2$	7722.8
$Li_{0.4}CoO_2$	7722.8
$Li_{0.4}CoO_2$	7721.6
$Li_{0.4}CoO_2$	7721.0
$Li_{0.4}CoO_2$	7721.2

Table 2. NEXAFS White Line Positions

Reproduced with permission of the copyright owner. Further reproduction prohibited without permission.

The integrated intensity of the small pre-edge peak occuring around 7704 eV is plotted in Fig. 18 as a function of Li-content. The weak pre-edge absorption is attributed to the dipole forbidden $1s \rightarrow 3d$ transition, and its intensity provides a measure of the degree of departure from octahedral coordination symmetry for the Co site. The trend of decreasing symmetry with increasing Li content is monotonic, even including an excess Li sample prepared by sol-gel techniques. Departure from the trend is noted for the $Li_{0.4}CoO_2$ sample, and is again, attributed to the structural phase transition which occurs at the lower lithium content (x = 0.5) [57].

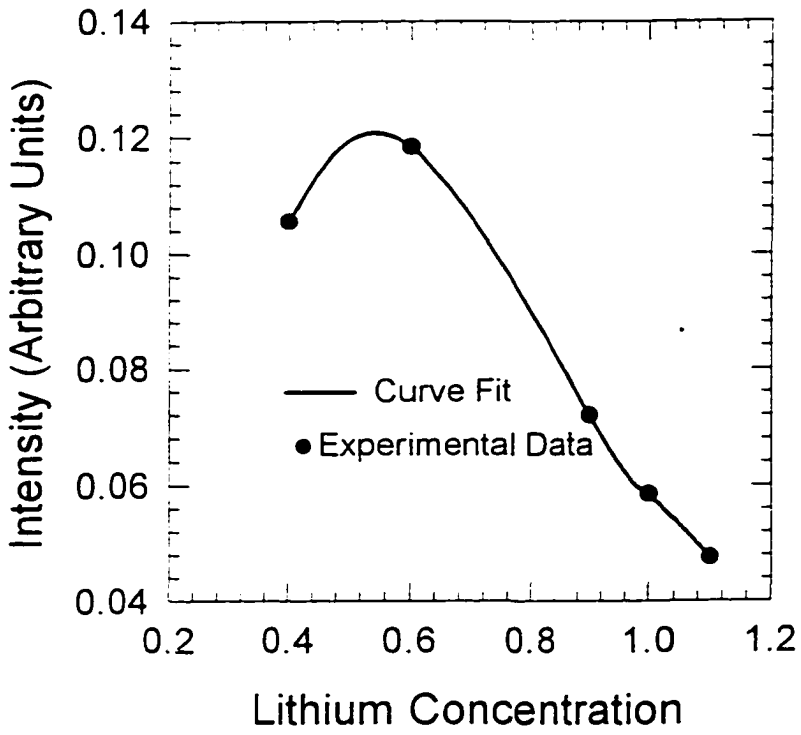

Figure 18 Plot of pre-edge integrated intensity vs. Li content

Reproduced with permission of the copyright owner. Further reproduction prohibited without permission.

3.2 $LiMn_2O_4$ Battery Cathodes [58]

The manganese K-edge x-ray absorption spectrum of the stoichiometric Arthur D. Little (ADL) sample is displayed in Fig. N. The pre-edge region due to $1s - 3d$ transitions, main edge jump, white line peak and first several EXAFS peaks are evident. Fig. N shows the white line peaks of several different stoichiometric $LiMn_2O_4$ obtained from three different commercial sources and the ADL process. Also included are commercial $LiMnO_2$ (Cyprus-Foote) and the Li-deficient material $Li_{0.7}Mn_2O_4$ (prepared starting with the ADL stoichiometric material). The positions of the peak maxima are listed in Table M. All of the stoichiometric $LiMnO_2$ samples have broad peaks centered at about 6562.0 eV. Small differences in Table M are within experimental uncertainty. (± 0.1 eV). The $LiMnO_2$ sample exhibits a main peak at lower energy, but with a component shoulder at about the same position as in $LiMn_2O_4$. The presence of a higher energy shoulder suggests that this sample is not a single-phase material. The results can be understood simply in terms of the different nominal Mn valencies in the two materials, Mn^{+3} and $Mn^{+3.5}$ in $LiMnO_2$ and $LiMn_2O_4$, respectively. Of course the latter represents an average between Mn^{+3} and Mn^{+4}. These results are also consistent with those reported for a series of manganese oxides

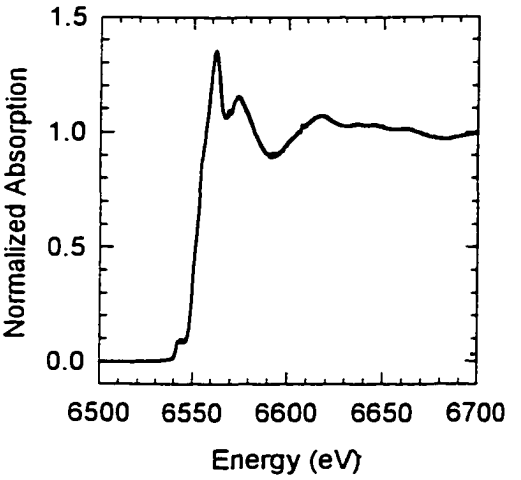

Figure 19 Manganese K-edge NEXAFS spectra in $LiMn_2O_4$ Arthur D. Little made samples.

Reproduced with permission of the copyright owner. Further reproduction prohibited without permission.

[59]. The NEXAFS spectrum of the Li-deficient material exhibits two interesting features. The first is the dramatic shift (about 1.5 eV) of the main peak to

Compound / Source	White Line Peak (eV)
$Li_{0.7}Mn_2O_4$ (ADL)	6563.4
$LiMn_2O_4$ (CF)	6562.0
$LiMn_2O_4$ (CM)	6561.8
$LiMn_2O_4$ (IBA)	6561.6
$LiMn_2O_4$ (ADL)	6561.8
$LiMnO_2$ (CF)	6558.7

Table 3. NEXAFS peak maxima

higher energy. This is attributed in part to the increase in charge on the Mn ion caused by the removal of compensating electronic charge associated with the lithium deficiency. This relatively large shift is consistent with the expectation that the compensating electrons come mostly from the Mn *d*-orbitals rather than from the generation of defect oxide species. The second feature of note is the clear low energy shoulder in the spectrum, occuring at about 6557 eV, which is attributed to the presence of Mn^{+2}. This assignment is based on published NEXAFS data for MnO [60]. Thus it seems that the new ADL process for obtaining $LiMnO_2$ is an improvement is over the older technologies with regards to the unwanted presence of a Mn^{+2} phase.

Reproduced with permission of the copyright owner. Further reproduction prohibited without permission.

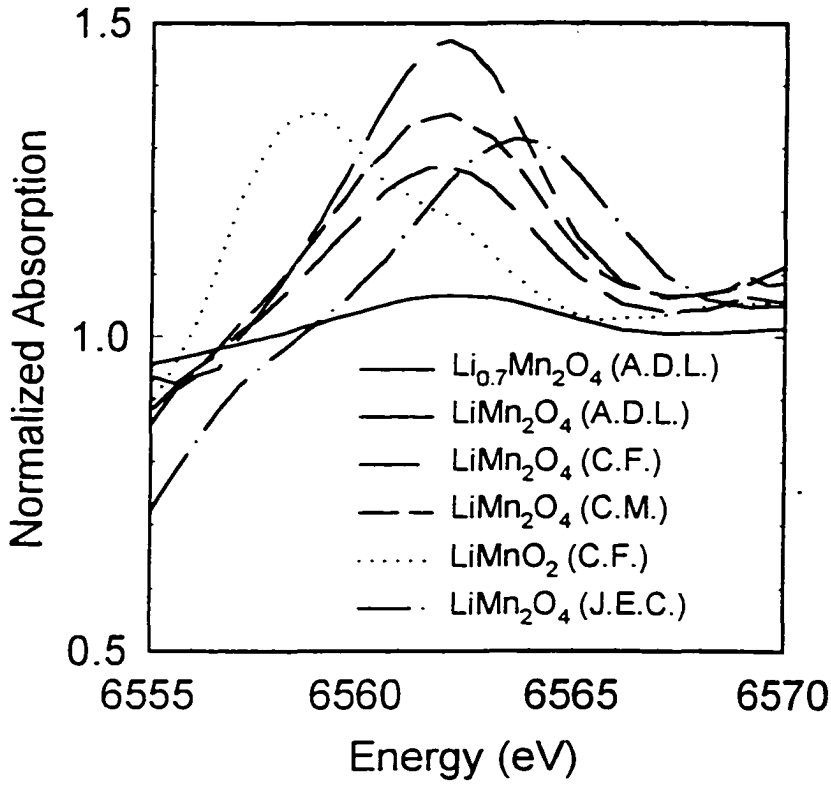

Figure 20 White line peaks of $LiMnO_2$ obtained from different sources.

Reproduced with permission of the copyright owner. Further reproduction prohibited without permission.

3.3 $Li_xV_6O_{13}$ Battery Cathodes [61]

Sample Preparation

Polycrystalline $Li_xV_6O_{13}$ samples with $x = 0, 0.5, 1, 1.5, 2, 3, 4, 5$, and 6 were prepared using V_6O_{13}, fabricated using a thermal decomposition process of NH_4VO_3 detailed in [2]. Chemical intercalation was performed in 25 ml glass bottles sealed with a teflon-silicon septum through which n-butyl lithium (Merck, 1.6 M in hexane) was added with a Hamilton syringe. The reaction was stopped after 20 hours by evaporating the hexane with flowing argon. The major difficulty in this work has been controlling the amount of intercalated lithium. With this process some of the lithium participates in the formation of a number of lithium and oxygen deficient impurity compounds. The type and amount of impurity have a direct impact upon lithium intercalation and the overall performance of V_6O_{13} as a cathode material. It is possible for the V_6O_{13} batch to be slightly non-stoichiometric (i.e. $V_6O_{12.9}$), but the amount of impurity in the final product is primarily due to the quality of the n-butyl lithium. Samples for spectroscopic measurement were prepared under controlled conditions in a dry glove box to prevent exposure to atmospheric water. For EPR and NMR, samples were sealed into quartz tubes. For x-ray absorption, for which quartz would absorb too strongly, they were sealed into paraffin and kapton tape.

1. Near-Edge (NEXAFS) Region

Near-edge x-ray absorption fine structure (NEXAFS) and extended x-ray absorption fine

Reproduced with permission of the copyright owner. Further reproduction prohibited without permission.

structure (EXAFS) measurements of the vanadium K-edge were made at room temperature in transmission at beam line X-23B at the National Synchrotron Light Source at Brookhaven National Laboratory using a double Si(111) crystal monochromator. The energy resolution was typically ~ 0.5 eV, although smaller shifts could be detected by the use of a reference sample. As is customary, all spectra were normalized to the main edge jump.

Fig.21(a) shows the overall vanadium K-edge spectra of $Li_xV_6O_{13}$ for various x. The main absorption edge appears at about 5475 eV. The "pre-edge" region before the main edge is shown on an expanded scale in Fig. 21(b). This pre-edge has been shown to be due to $s \rightarrow d$ transitions which, while dipole-forbidden, become allowed in non-octahedral symmetry as the vanadium $3d$ states mix with the oxygen p states [62]. Therefore the strength of this transition, which may be measured by integrating the area of the peak above background, is proportional to the deviation from local octahedral symmetry of the vanadium site [63]. It is evident from Fig. 21(b) that the transition strength in general first increases for increasing x and then decreases rapidly for $x > 1.5$. The structural changes implied by these results are corroborated by EXAFS analysis and further discussed below.

The "white line" peak after the edge jump gives additional information about the chemical environment of the vanadium. The white line intensity is proportional to the number of $1s \rightarrow np$, $n = 4, 5, \ldots$, transitions, so it in effect probes unoccupied p symmetry final states [64]. There may also be localized exciton levels occasioned by the screening of the core hole [65]. The white line peak is shown expanded in Fig. 3(c) as a function of x. Clearly, this peak is larger at high Li concentration. At low Li concentrations, $0 < x < 1$, i.e, higher vanadium oxidation states, the white line exhibits a possible ligand splitting effect [66].

Reproduced with permission of the copyright owner. Further reproduction prohibited without permission.

As shown in Fig. 21, both the pre-edge peak and the main absorption.edge shift to lower binding energy with increased lithium content. Addition of electrons to vanadium lowers the effective binding energy of the electrons at the vanadium site and better screens the core hole produced in the x-ray absorption event. The observed shift is due to the reduction of the formal valence of vanadium on addition of lithium, from 4.33 for $x = 0$ to 3.33 for $x = 6$. In a mixed-valent material like $Li_xV_6O_{13}$, the shift is an average over the V^{5+}, V^{4+} and V^{3+} species. This shift, which attains its largest value of ~1 eV for $x = 6$, is plotted in Fig. 4 along with a linear fit to the position of the pre-edge for several reference compounds in which vanadium has an integer valence, namely V_2O_5, V_2O_3 and VO_2. This reference data is in good agreement with previous studies of vanadium oxides [13].

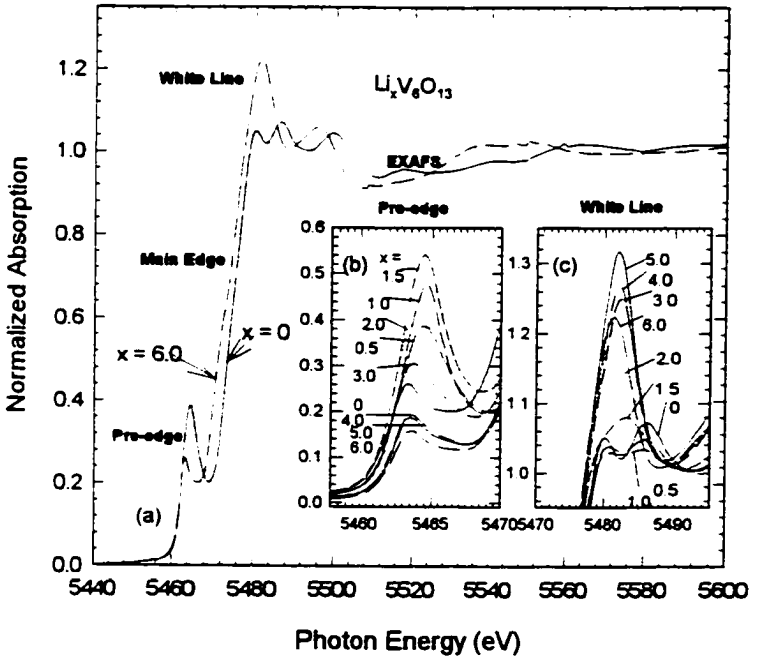

Figure 21 (a) Near-edge XAS spectrum of the V 1*s* edge LixV6O13 samples, and on an expanded scale, (b) the pre-edge peak and (c) the WL region

The vanadium oxidation state in the $Li_xV_6O_{13}$ samples deviates from stoichiometrically xpected values for $0.5 < x < 1.5$ (greater than expected) and $2 < x < 4$ (less than expected). These deviations are due to lithium deficient and oxygen deficient impurity compounds (Li_zVO_y) formed during the intercalation process and VO_y impurity compounds that may exist in the V_6O_{13} starting material. At large lithium contents, oxygen deficient impurities provide the excess V^{3+} content. By calculating the difference

Reproduced with permission of the copyright owner. Further reproduction prohibited without permission.

between the mean vanadium oxidation state for the measured and expected values (Fig. 22), we can estimate the oxygen deficient impurity content. The fraction of vanadium atoms associated with oxygen deficient impurities is found to range between ~0% (x = 5 and 6) and 35% (x = 3), the latter being an upper bound which overestimates the true content.

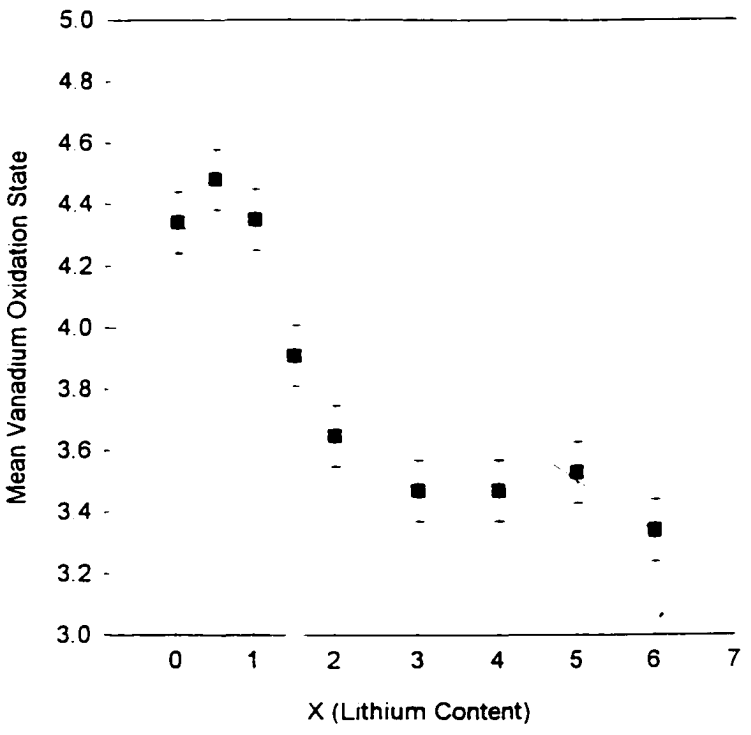

Figure 22 Mean vanadium oxidation number vs. lithium content (x): (closed squares); straight line denotes the mean oxidation state for "ideal" $Li_xV_6O_{13}$.

2. Extended Region (EXAFS)

The extended x-ray absorption fine structure (EXAFS) above the vanadium K edge gives structural information about the local geometry around the vanadium atoms, as well as the distances to near neighbor atoms and the number of such atoms in each coordination shell. We have measured the local structure for the stoichiometric compound, V_6O_{13}, and measured deviations from it as a function of Li content.

To extract the EXAFS from the measured absorption spectrum it is necessary to remove the relatively smooth background atomic absorption μ_o. To approximate this background we have used the routine AUTOBACK. The signal was weighted by k^3 to compensate for attenuation with increasing k (Fig. 5(a)). The resulting oscillations were Fourier transformed and the amplitude of

Reproduced with permission of the copyright owner. Further reproduction prohibited without permission.

the transform (FTA) is plotted in Fig. 5(b). Peaks in this function correspond to interatomic spacings in the vicinity of the vanadium atom.

We now describe the fitting of these measured features to calculated functions. Single crystal and powder x-ray diffraction studies have shown that V_6O_{13} consits of layers of VO_6 octahedra [67]. Using reported lattice constants and interatomic distances [68] we calculate an EXAFS spectrum, using the package FEFF 6.01. The results are then compared with experimental data. There are three inequivalent vanadium sites in the unit cell with V-O bond distances in the first coordination shell ranging from 1.64 to 2.28 Å. Further shells are closely spaced and are not resolved in the FTA plot. For instance, the third major peak (Fig. 5b) is due to both V-V and V-O distances. The theoretical spectrum thus generated was fitted to the experimental data in *r* space. Fitting in *r* space has the advantage that the amplitude function has a direct physical interpretation, as it is related directly to interatomic spacings. In Fig. 5(b) we compare the best fit multiple shell functions to the experimental FTA for V_6O_{13}.

To obtain a good fit it is necessary to incorporate multiple-scattering paths in the simulated spectrum. Some 100 paths (~30 for each of the three *inequivalent* vanadium sites (Ref.) are required. The Debye-Waller is a fitting parameter here, but can be derived from dynamic and static disorder effects [69]. Generally, the overall σ^2 can be written as a sum of two terms, a vibrational and disorder one (Eq. To separate the vibrational (temperature dependent) part from the static part, measurements must be taken at various temperatures. In the case of V_6O_{13} the best fit function assumes an explicit dependence of σ^2 (r) on the separation between absorbing atom and backscatterer. This separation includes the effective length of multiple scattering paths. We find that $\sigma^2 \sim (r_{eff})^{r_{eff}}$, where r_{eff} is the effective scattering path length. This dependence indicates strong static

Reproduced with permission of the copyright owner. Further reproduction prohibited without permission.

disorder beyond the first shell, possibly due to defects in the host lattice. The effect of impurities on the lattice significantly complicates the EXAFS, so our evaluation is confined to lithiated samples with smaller impurity contents (i.e. x = 0, 4, 5 and 6).

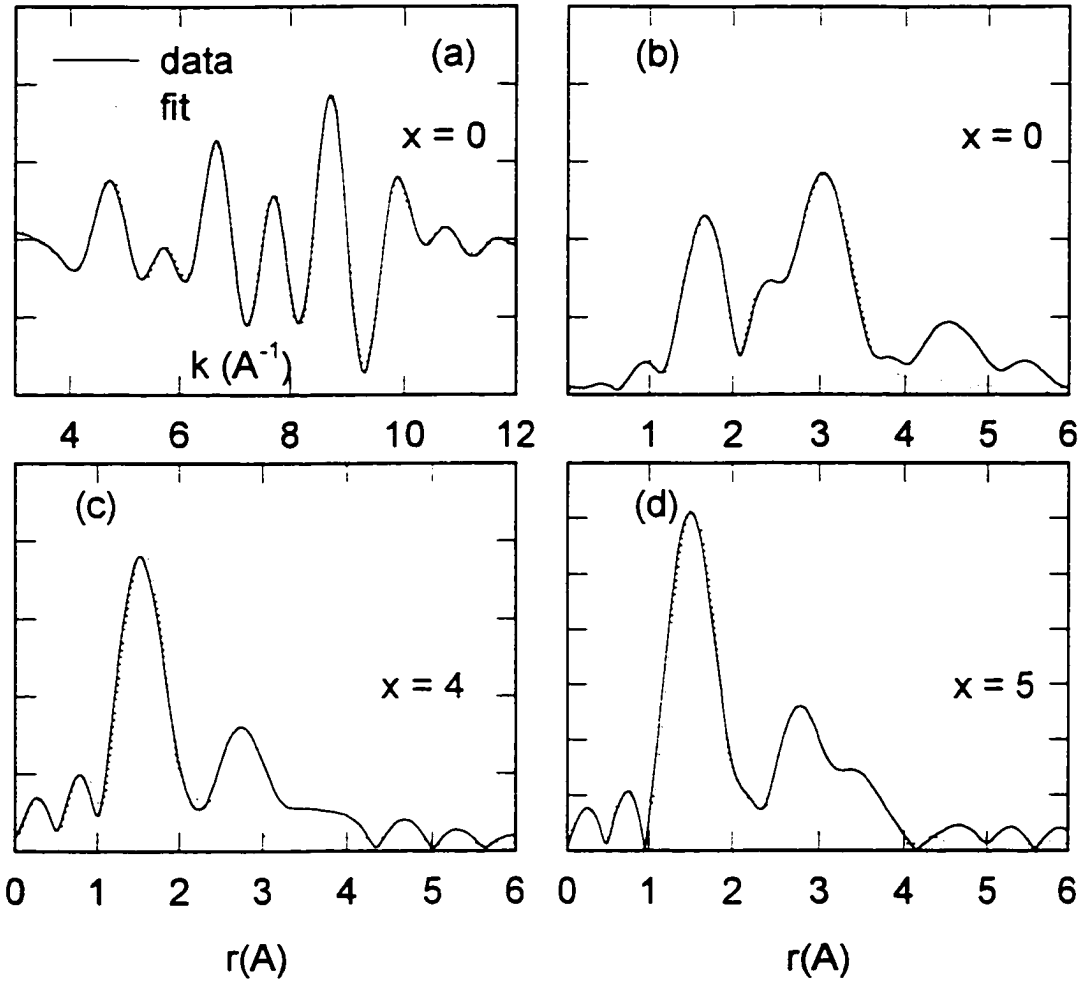

Figure 23

k^3 weighted V_6O_{13} EXAFS spectrum (b)-(d) Fourier transform amplitude (FTA) of the EXAFS of V_6O_{13} (solid lines), compared to the the simulation results (dotted) as described in the text for x = 0, 4, 5.

Reproduced with permission of the copyright owner. Further reproduction prohibited without permission.

Important trends are apparent from the behavior of the EXAFS as a function of lithium content. As shown in Fig. 24(a), the first EXAFS oscillation in energy space shifts as a function of x, reflecting the expansion of the first-shell octahedron. In addition, the intensity and sharpness of the first FTA peak (Fig. 24(b)), which corresponds to the V-O distances in the first octahedron, increases with x. This implies that there is a decrease in the distribution of first shell V-O distances. This means that the bond distances become more equivalent, i.e. the VO_6 octahedra become less distorted. This is corroborated by the fact that the first FTA peak can be well fit using a single shell model, i.e. equal V-O distances, as shown in Fig. 5(c) and 5(d) for $x = 4$ and $x = 5$. This EXAFS measurement confirms the behavior of the pre-edge intensity with increasing x discussed earlier, e.g. Fig 3(b). The pre-edge intensities and the first RDF peak amplitudes are plotted in Fig. 7(a). There is good agreement between these measurements at every value of x. Even though both sets of data are part of the same absorption spectrum, they are due to different electronic transitions within the V ion and therefore are semi-independent measurements of changes in the vanadium environment. Both sets

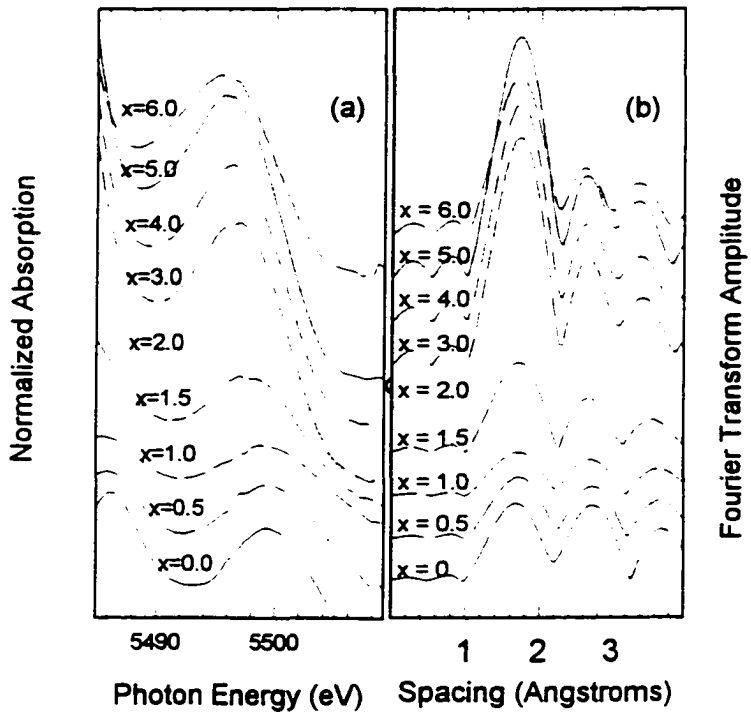

Figure 24
(a) Relative position of first EXAFS oscillation for different values of x in LixV6O13. (b) comparison of FTAs as functions of x showing an increase in amplitude and sharpness of the first peak due to V-O

Reproduced with permission of the copyright owner. Further reproduction prohibited without permission.

of data suggest the existence of three distinct structural regimes. For $x \leq 1$ there is a slight increase in the distortion from octahedral symmetry with increasing x; for $1 < x \leq 3$ there is a dramatic decrease in the octahedral distortion; and for $x > 3$ the vanadium octahedra undergo no further change.

However, the long-range structure is increasingly compromised (becomes more disordered) with lithium content. A qualitative measure of long-range disorder is obtained by taking the ratio of peak 1 to peak 2 in the FTA. Fig. 7(b) shows that the disorder begins to increase around x = 1.0; it increases most rapidly to about x = 2.0 and thereafter increases modestly up to x = 6. It is likely, when the impurity content is large, as with samples $1 \leq x \leq 3$, that the disorder is increased. The increase in symmetry of the first-shell octahedra and the corresponding increase in disorder at longer distances are not surprising considering the structural changes that must

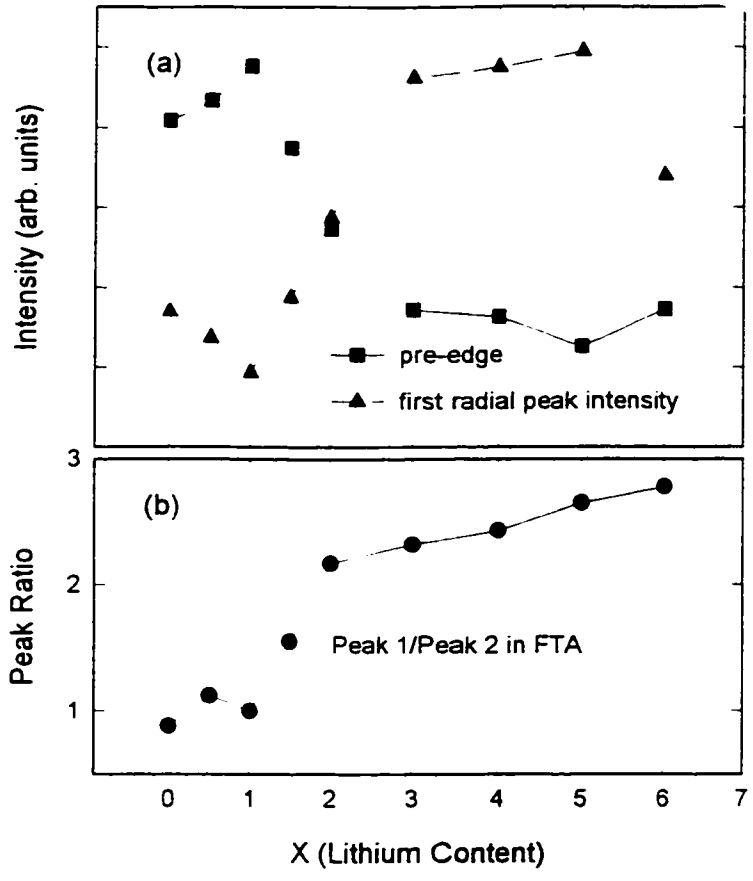

Figure 25

Different measurements of the structural changes around the V ions in $Li_xV_6O_{13}$ (a) Decreases in the pre-edge intensity and increases in the amplitude of the first V-O peak in the FTA; both reflect the increases in the local octahedral symmetry with x. (b) The ration of the first to the second FTA peak increases with x, reflecting increasing disorder.

Reproduced with permission of the copyright owner. Further reproduction prohibited without permission.

occur upon lithium intercalation.

Quantitative estimation of the expansion of the lattice become difficult as long-range disorder increases. In addition the V_6O_{13} structure is anisotropic. The expansion of the lattice, therefore, cannot be completely measured by an angularly averaged polycrystalline spectrum. However, on the basis of the expansion observed in the first V-O shell , which approaches 2.11±0.2Å at $x = 5.0$ compared to 1.93±0.3 Å for V_6O_{13}, we can crudely estimate a 5 - 10 % increase in the lattice parameters. This agrees with estimates based on x-ray diffraction analysis 70. Similar lattice expansions are observed with other vanadium oxide compounds on lithium intercalation 71. It is interesting to note that a lattice contraction occurs for Li_xCoO_2 on lithium intercalation for $x < 1$. This is explained as a screening effect by the interstitially located Li^+, effectively lowering the coulombic repulsion between the oxygen and host ions [72].

2. Electron Paramagnetic Resonance (EPR) Measurements

EPR measurements were performed at room temperature on an IBM/Bruker ER-220 X-band EPR spectrometer. EPR spectra were obtained in single field-sweep mode. Spectral intensities were corrected for effects due to varying receiver gain and/or microwave power on each sample

X-band EPR spectra for $Li_xV_6O_{13}$ are shown in Fig. 26. The nominal vanadium valence for $x = 0$ is 4.33, which is the average of the stable 4+ and 5+ states. Intercalation of Li^+ reduces the vanadium valence by initially creating more V^{4+}. However, since the room temperature EPR signal is dominated by the paramagnetic 4+ state, the integrated intensity will reflect the amount of V^{4+}. The EPR signal steadily increases to its maximum value for $x = 1.5$, which corresponds to the highest V^{4+}

Reproduced with permission of the copyright owner. Further reproduction prohibited without permission.

concentration (nominally 100%). When x increases to 2, the spectrum becomes very broad (with some intensity apparently outside the observation window of 0.5 T) due to strong magnetic dipole-dipole interactions. With the addition of Li beyond x = 2, the EPR signal decreases. In addition, splitting of the EPR line is observed for $x \geq 4$, suggesting the presence of more than one structural phase, as further discussed below. At room temperature and 3 cm microwave wavelength, the V^{3+} contribution to the EPR line (expected at higher Li content) is weak. We attribute this to relatively large zero-field splittings and very short relaxation times 73.

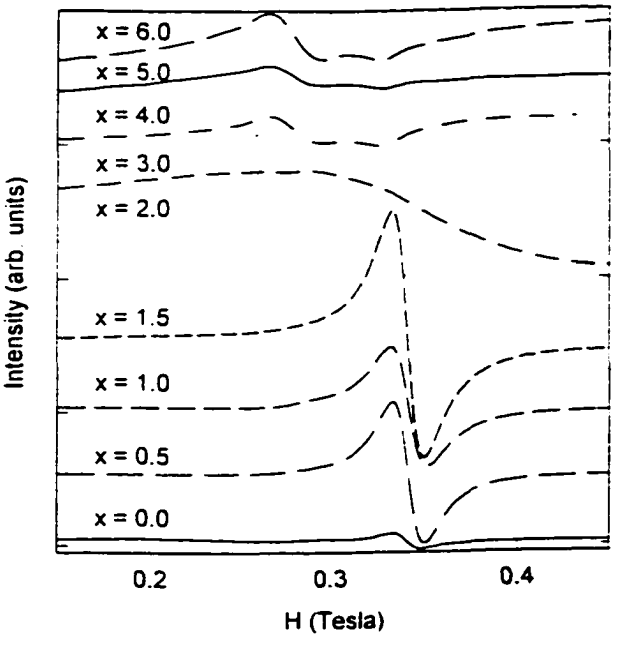

Figure 26 Electron paramagnetic resonance spectra of $Li_xV_6O_{13}$ samples.

Conclusions

The combination of EPR and x-ray absorption spectroscopy of the vanadium oxide host and NMR of the lithium intercalant (which lies outside the scope of this dissertation) has given a comprehensive view of the changes in electronic, magnetic and structural properties which accompany lithium intercalation into V_6O_{13}.

We illustrate in Fig. 27 a convenient way of visualizing the continuum of vanadium oxidation states on intercalation of lithium into V_6O_{13} as appropriate mixtures of V_6O_{13}, $Li_2V_6O_{13}$ and

Reproduced with permission of the copyright owner. Further reproduction prohibited without permission.

$Li_8V_6O_{13}$, compounds with mean vanadium oxidation numbers of 4.33, 4 and 3 respectively. Ideally, each intercalated lithium atom is accompanied by a conversion of V^{5+} to V^{4+} until all V^{5+} is exhausted and the composition $Li_2V_6O_{13}$ is reached. Subsequently, the conversion of V^{4+} to V^{3+} commences until the composition $Li_8V_6O_{13}$ is reached. The plausibility of this simple scheme is corroborated by our results.

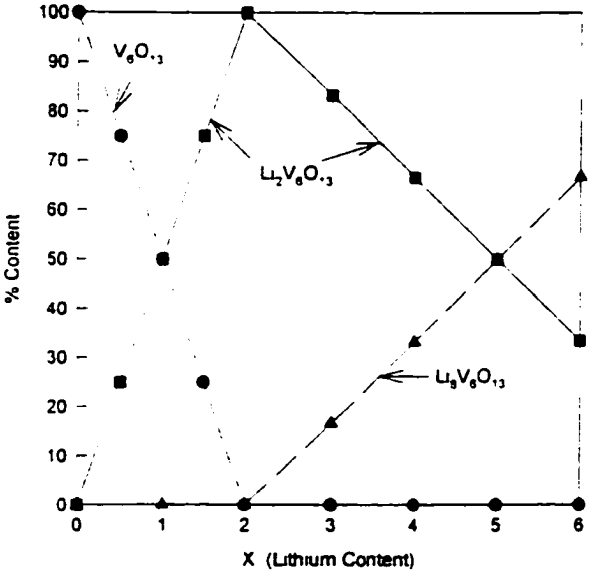

Figure 27

"Ideal" LixV6O13 compounds as mixtures of V_6O_{13}, $Li_2V_6O_{13}$ and $Li_8V_6O_{13}$ components. The results of the combined XAS, EPR and ^{17}Li NMR analysis (not discussed in the text) support such a scheme, notwithstanding the specific complications due to sample preparation and purity of phase of the starting material (Ref. 67).

Reproduced with permission of the copyright owner. Further reproduction prohibited without permission.

3.4 $LiNiO_2$ Battery Cathodes [74]

Each powder sample was carefully sealed between two layers of wax paper in a dry glove box to isolate it from atmospheric moisture. Near-edge x-ray absorption fine structure (NEXAFS) and extended x-ray absorption fine structure (EXAFS) measurements of the Ni K-edge were made at room temperature in transmission at beam line X-23A2 at the National Synchrotron Light Source at Brookhaven National Laboratory using a double Si(311) crystal monochromator. The energy resolution was typically ~ 0.5 eV, although smaller shifts could be detected by the use of a reference sample. All spectra were normalized to the main edge jump.

The extended range modulation in the absorption spectrum (50 eV-900 eV above the edge) measures the backscattering of the photoelectron from the first several coordination shells centered at the absorbing Ni site. Analysis of this spectral range can give information regarding the spacing (R), coordination number (N), and disorder ($\Delta\sigma^2$) of each shell. We have focused on measuring the structure of the first (Ni-O) and second (Ni-Ni) coordination shells in

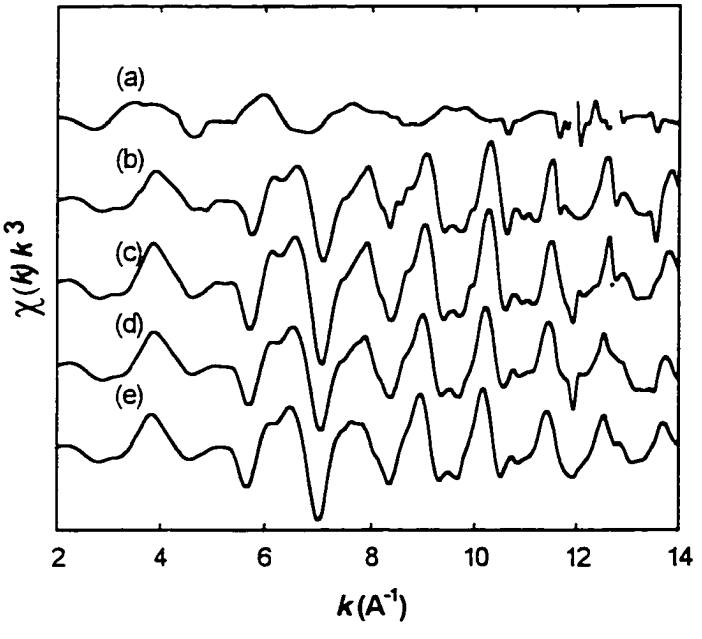

Figure 28 EXAFS k^3 weighted spectra of Ni compounds a) precursor, b) $LiNiO_2$, c) $LiNiO_2$ (5% Li), c) $LiNi_{0.75}Co_{0.25}O_2$ d) $LiNi_{0.75}Co_{0.25}O_2$ (5% Li)

Reproduced with permission of the copyright owner. Further reproduction prohibited without permission.

the $Li(Ni,Co)O_2$ samples and the Ni-O shell in the precursor sample, which is the only resolved interaction in the latter material. Fig. 2 shows the background subtracted *k* space EXAFS spectra for the $Li(Ni,Co)O_2$ series. All spectra are weighted by k^3 to compensate for decrease in amplitude with increase in *k* (Fig 2). The useful Δk range was found to be from 3 Å to 14 Å, which allows a resolution (ΔR) of $\pi/2\Delta k$ or $\Delta R \geq 0.14$Å. The precursor spectrum is significantly less structured than in that of the other samples. This indicates the Ni environment in the precursor is highly disordered, as discussed further below. In order to determine the structural parameters in the first and second shells we have fitted simulated spectra (FEFF 6.01[75]) to the experimental data. The simulations were based on the well-known $LiNiO_2$ crystallographic parameters.[76] The first shell was assumed to consist of six oxygen atoms at trial distances of 2.02 Å and the second of six Ni atoms at 2.87 Å. The first Ni-Li interaction was neglected due to the weak Li backscattering. In order to simulate the $LiNi_{0.75}Co_{0.25}O_2$ spectra, ideal Co substitution for Ni was assumed. Theoretical phase and amplitude functions for a Ni-Co distance of 2.87 Å were calculated and combined with Ni-Ni in a 1:4 amplitude ratio.

1. Near Edge

Fig. 3a shows the Ni K absorption edge for the $Li(Ni, Co)O_2$ samples and two Ni standards, Ni metal and NiO. It is apparent that the edge energy of the $LiNiO_2$ is lower than that in the $LiNi_{0.75}Co_{0.25}O_2$. The shift toward higher binding energies in Ni oxycompounds is linearly related to the increase in the mean oxidation state of the Ni ion as shown by Mansour and Melendres.[77] Using a different calibration procedure, in which the first derivative maximum was plotted against

Reproduced with permission of the copyright owner. Further reproduction prohibited without permission.

the oxidation numbers of stoichiometric standards (Fig. 30), we have extrapolated the average valency in the mixed compounds (Table 4). The value of this chemical shift ΔE per electron, while larger than that observed in Ref. 77, is similar to that reported in a study of various cobalt compounds.[78] The mean oxidation state of stoichiometric $LiNiO_2$ was taken to be +2.7 which is the value reported in Ref. 77. The small increase in average Ni valency in the cobalt substituted compounds shown in Table 4 is actually a lower bound for this effect, as it is slightly dependent on the extrapolation procedure. A different calibration scheme using the inflection point of the main edge jump yields a value closer to 2.9 for the cobalt substituted samples and no

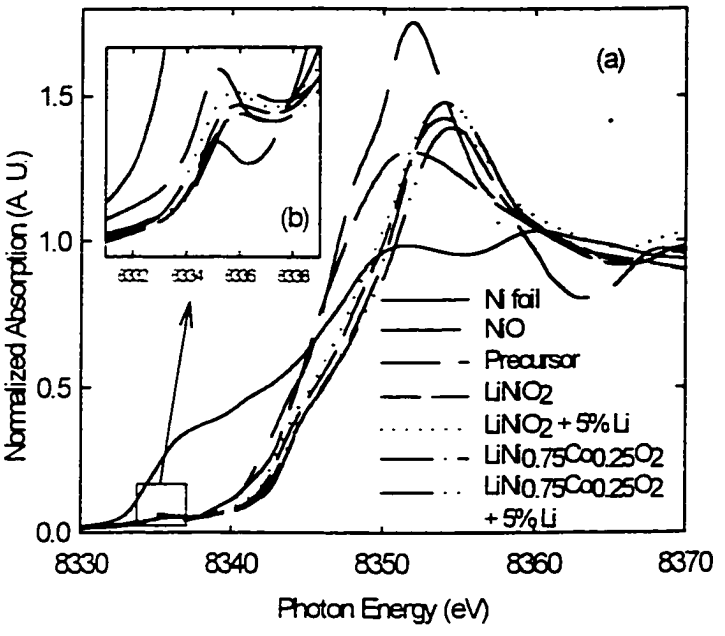

Figure 29 a) Ni 1*s* edge and b) pre-edge absorption peak in the Ni compounds indicated.

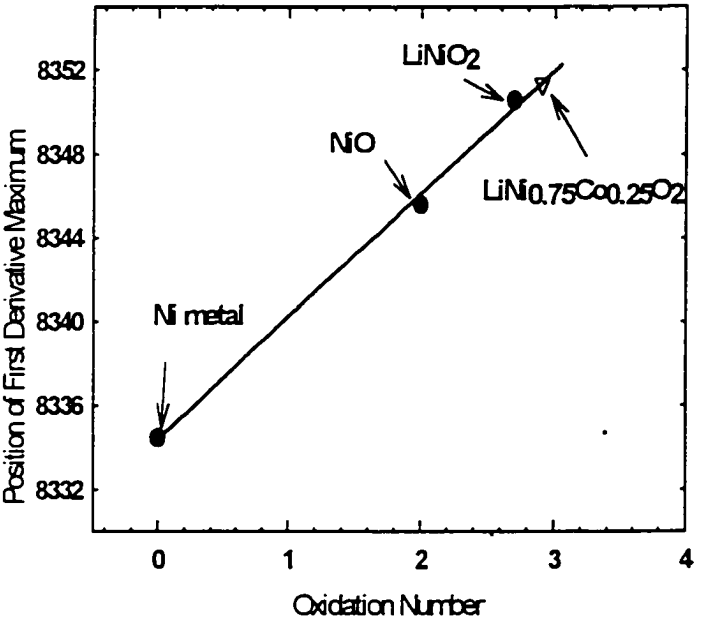

Figure 30 Position of Ni 1*s* absorption edge in $LiNi_{0.75}Co_{0.25}O_2$ and stoichiometric compounds indicated.

Reproduced with permission of the copyright owner. Further reproduction prohibited without permission.

change in the excess lithium $LiNiO_2$ one. Thus it appears that Co substitutes preferentially for Ni^{2+}, thereby increasing the average Ni valence.

The small pre-edge peak (Fig. 29b) is due to $1s \rightarrow 3d$ transitions which are dipole-forbidden in a central symmetric site. Deviations from octahedral symmetry at the Ni ions give rise to this peak, the intensity of which is therefore a measure of the distortion of the NiO_6 octahedra. From Fig. 3b it is apparent that the pre-edge peak positions in $LiNiO_2$, $LiNiO_2$ +5% Li, $LiNi_{0.75}Co_{0.25}O_2$ and $LiNi_{0.25}Co_{0.25}O_2$ +5%Li are very close and are shifted ~0.6 eV above the NiO and precursor peak positions, consistent with Ref. 8. The precursor pre-edge peak is also somewhat sharper than that of the product samples.

Sample	Position of Edge (First Deriv. Max)	Average Ni Oxidation State
Precursor	8345.8	1.98
$LiNiO_2$ (5%Li)	8350.5	2.72
$LiNi_{0.75}Co_{0.25}O$	8351.3	2.82
$LiNi_{0.75}Co_{0.25}O$ (5%Li)	8351.2	2.81

Table 4. Edge position and average Ni oxidation state

2. Extended range

Fig. 31 gives the Fourier transformed spectra and the best fit simulation curves to these spectra. The peak positions are related to interatomic distances. The best values of the floating

Reproduced with permission of the copyright owner. Further reproduction prohibited without permission.

parameters in the fit are given in Table 5 along with the quality of the fit, expressed in terms of the normalized least squares residual χ^2_ν. Because the limited range of the data and the high degree of correlation between the free parameters leads to instability in the fits, not all parameters were varied simultaneously. The distortion of the NiO_6 octahedra in lithiated Ni oxides has been interpreted by Pickering *et al.*[79] as related to the mixed valence of Ni, namely Ni^{+2} and Ni^{+3}. The Ni-O shell in the stoichiometric sample involved, in good agreement with previously reported results,[8] two types of Ni-O bonds, four short ones at 1.91 Å and two long ones at 2.06 Å. In that study[8] these various bond lengths were assigned to different Ni-O interactions, short bonds corresponding to Ni^{+2}-O^{-} and Ni^{+3}-O^{-2} and long ones corresponding to Ni^{+2}-O^{-2}. The formal oxidation state was therefore less than the edge shift extrapolated one of 2.7. We observe a shift in the cobalt substituted compounds with no change in the ratio or values of the Ni-O separation compared to stoichiometry. Both $LiNiO_2$, $LiNiO_2$ +5%Li, $LiNi_{0.75}Co_{0.25}O_2$ and $LiNi_{0.25}Co_{0.25}O_2$ +5%Li are characterized by the same distortion of the NiO_6 octahedra. If the increase in average Ni valency, as indicated by the measured edge shift, leads to a predominantly Ni^{+3} environment, a measurable decrease in the distortion of the NO_6 octahedra

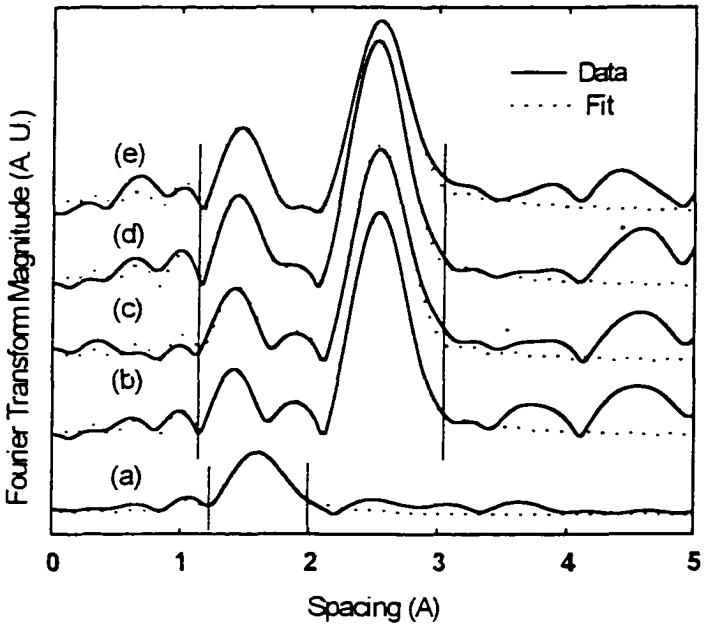

Figure 31 Fourier transform EXAFS amplitudes (not adjusted for phase shifts) for: a) precursor; b) $LiNiO_2$; c) $LiNiO_2$ + 5% Li; d) $LiNi_{0.75}Co_{0.25}O_2$; e) $LiNi_{0.75}Co_{0.25}O_2$ + 5% Li.

Reproduced with permission of the copyright owner. Further reproduction prohibited without permission.

in all of product samples would be expected. Apart from the resolution and precision concern, the fact that no such decrease was measured could be attributed to a distortion characteristic of a purely N^{+3} environment. Such a Jahn-Teller type distortion attributed to the low $t_2^6e^1$ spin state of the N^{+3} ion has been measured by Rougier *et al.*[80] in a quasi 2D system of nearly pure trivalent Ni. The values obtained for the different Ni-O bond lengths and their ratio is identical to the ones measured for a presumably mixed valence $LiNiO_2$ system in which the distortion is related to the difference in ionic radii of the divalent and trivalent Ni. In the precursor a single Ni-O distance gives the best fit, implying that this first shell distortion is absent from this material. The bond lengths are consistent with the +2 Ni valency measured in the edge shift. Further coordination shells are strongly disordered and no fitting was attempted.

Reproduced with permission of the copyright owner. Further reproduction prohibited without permission.

Sample	Shell	S_0	N	R	$\Delta\sigma^2$	E_0	χ^2_ν
Precursor	Ni-O	0.46	6	2.06	0.005	-7.2	44
$LiNiO_2$	Ni-O	0.71	4	1.91	0.003	-10.8	17
	Ni-O	0.71	2	2.06	0.005	-10.8	17
	Ni-Ni	0.71	6	2.89	0.005	-10.8	17
$LiNiO_2$ (5% Li)	Ni-O	0.71	4	1.91	0.004	-8.8	17
	Ni-O	0.71	2	2.05	0.005	-8.8	17
	Ni-Ni	0.71	6	2.89	0.005	-8.8	17
$LiNi_{0.75}Co_{0.25}O_2$	Ni-O	0.82	4	1.92	0.005	-9.8	7
	Ni-O	0.82	2	2.06	0.009	-9.8	7
	Ni-Ni, Ni-Co	0.82	6	2.87	0.005	-9.8	7
$LiNi_{0.75}Co_{0.25}O_2$ (5% Li)	Ni-O	0.51	4	1.92	0.003	-7.5	10
	Ni-O	0.51	2	2.07	0.007	-7.5	10
	Ni-Ni, Ni-Co	0.51	6	2.87	0.004	-7.5	10

Table 5. Best fit parameter values from Ni K edge EXAFS analysis

Reproduced with permission of the copyright owner. Further reproduction prohibited without permission.

3.5 $LiFeS_2$ Battery Cathodes [81]

Fi The Li/CPE/FeS_2 battery (CPE = composite polymer electrolyte) is a promising candidate for electric vehicle and energy storage applications. Its projected specific energy is over 170 Wh/kg (based on 2.5 e/FeS_2). Recently a small laboratory cell demonstrated over 300 full charge-discharge cycles. In this work synchrotron x-ray absorption measurements were performed on a series of sealed Li/CPE/FeS_2 cells (CPE based on PEO:LiI) charged or discharged to various potentials. The Fe K-edge measurements were made in transmission mode and include both the near edge (NEXAFS) and extended (EXAFS) regions. The former provides information regarding the effective valence of the Fe while the latter yields knowledge of the coordination geometry. Six cells with the following parameters were examined: (i) charged to 1.85 V and x = 0.5, where x represents the number of electrons associated with that particular charge state; (ii) charged to 2.05 V and x = 1.7; (iii) charged to 2.25 V and x = 2.0; (iv) discharged to 1.65 V and x = 1.4; (v) discharged to 1.25 V and x = 0.15, and (vi) discharged to 1.1

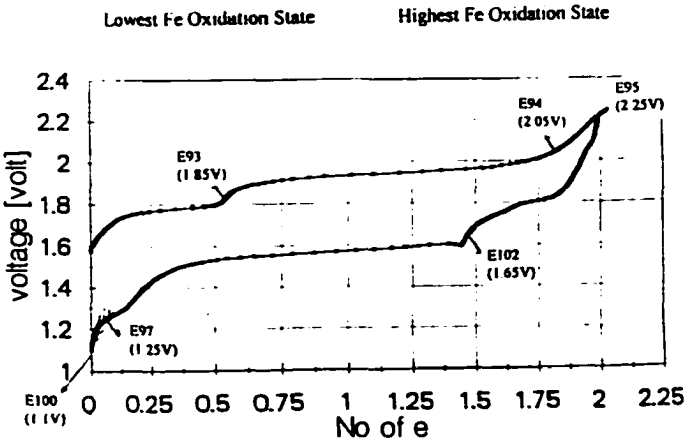

Figure 32
Charge/discharge curve for pyrite cathodes. The different points correspond to individual cell prepared at those values of the voltage and corresponding lithium content.

Reproduced with permission of the copyright owner. Further reproduction prohibited without permission.

V and x = 0.0 (Fig. 32).

Fig. 33 shows the near-edge x-ray absorption region for the cathode series. The six spectra fall into two distinct groups depending on which region of lithium content they belong to. The low lithium group exhibits a somewhat steeper edge jump compared to the high lithium one, combined with an obvious loss of structure in the near edge region. Such a distinct loss of structure has been attributed to the presence of a NiAs type $Fe_{1-x}S$ pyrrhotite at high lithium values in a similar FeS_2 cathode system [82], [83]. The overall edge position is also shifted to lower energies with the addition of lithium. This effect is well known and is attributed to the decrease in binding energy of the $1s$ electrons in the absorbing ion in conjunction with the lowering of the average oxidation of the latter. The derivative plot of the high lithium cathodes shows two distinct peaks corresponding to the shape and position of the sharp peak in metallic iron at ~ 7111 eV and the relatively broad one at ~7120 eV in the FeS_2 polycrystalline standard. This evidence of the coexistence of metallic iron and pyrite phases is confirmed by the extended range structure analysis. The small pre-edge feature is exhibits a sharper definition in the low lithium spectra. This pre-edge feature corresponds to $1s$ - $3d$ transitions, which are is dipole-

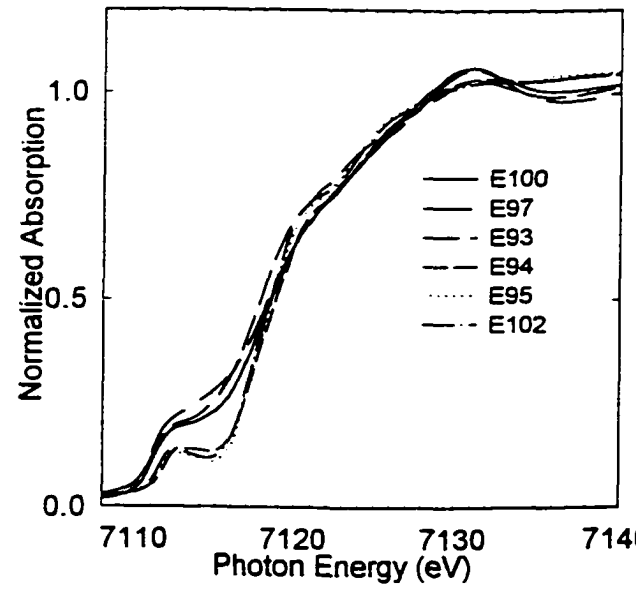

Figure 33
Pyrite cathode Fe K-edge spectra. The edges fall into two distinct groups depending at which part of the discharge curve the cathodes were prepared ("high" and "low" lithium content.)

Reproduced with permission of the copyright owner. Further reproduction prohibited without permission.

forbidden in octahedral symmetry, and its strength therefore indicates that the symmetry decreases as Li is removed from the cathode.

The k^3 weighted spectra for cathode series and the magnitude of the Fourier transform of the latter are shown in Fig. 34a and 34b. There is clear evidence of two entirely different structural environments centered at the absorbing Fe ion. The low lithium group demonstrates very little structure beyond the first peak around 2 Angstroms. The high lithium group on the other hand, shows a clear long range structure up to more than 5 Angstroms. The spectra within each group display the same features and imply a nearly identical Fe environment. The identification of the possible iron compounds formed under lithiation in the two types of cathodes was attempted using a least squares fit of theoretical FEFF 6.01 standards to the data. The fit was performed in r space. A linear combination of scattering paths corresponding to the coordination shells of several possible crystalline Fe compounds was used to simulate the data in the first approximation. The scattering distances and coordination numbers for all paths within clusters were kept constant in accordance with known crystallographic values. Debye-Waller factors, E_0, and overall scale factors were allowed to vary. The difference in the overall scale factors were attributed to different abundance of the chemical components and not to changes in coordination. This of

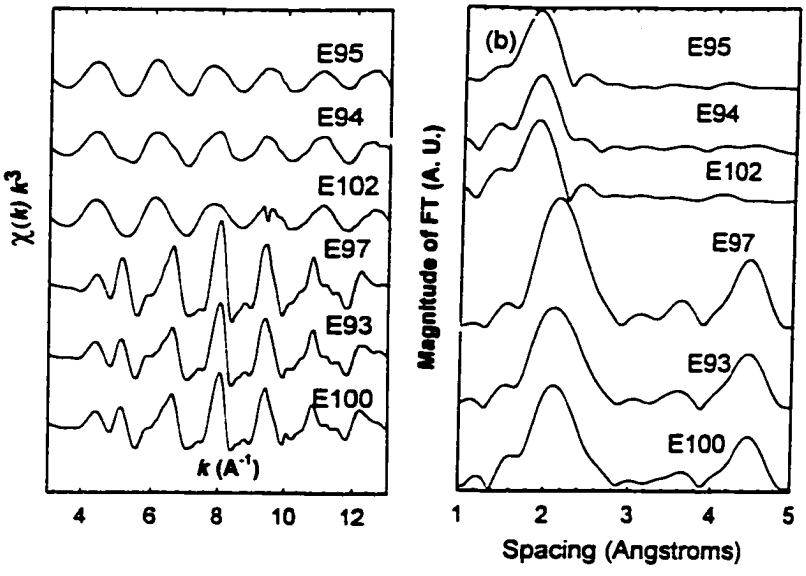

Figure 34 Pyrite cathode EXAFS spectra: (a) k space. (b) FTA

Reproduced with permission of the copyright owner. Further reproduction prohibited without permission.

course is only meaningful when the overall scale factors have been extracted from the fit to the same experimental standards. For that purpose we have fitted FEFF functions to several iron compounds including metallic iron, FeS and FeS_2.

The refined simulation of each spectrum in the high lithium group gave results, which are identical within the uncertainty of the fit. As shown in Fig. 4 for the E95 cathode best fit values were obtained from a combination of FeS_2 and metallic iron. The values for the Debye Waller factors which measure the random disorder about the ideal atomic positions were somewhat greater for the cathode fit at higher order FeS_2 shells compared to the fit to the experimental standard. This indicates an increase in static disorder with increasing distance within the coexisting pyrite phase. The metallic iron contributions are consistent with those calculated for the foil standard. The overall scale factors corresponding to the two structures which are free parameters in the fit, are corrected for by the corresponding ones from the fit to the experimental standards. The values, thus obtained, imply a 40% abundance of FeS_2 and 60% abundance of metallic Fe.

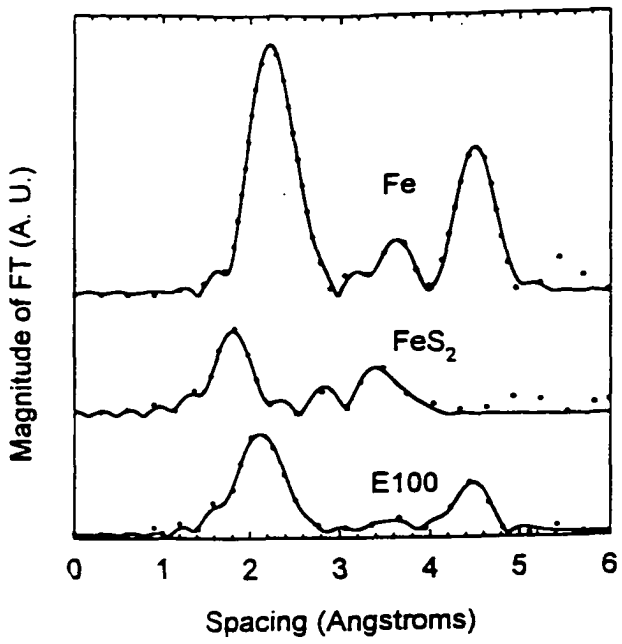

Figure 35
FTAs of K-edge EXAFS - experimental data and FEFF simulation fits for stoichiometric FeS_2, Fe metal and a representative "high lithium" cathode sample.

The fit to standards for the low lithium group, using fixed coordination numbers and atomic distances did not give reasonable results. Due to the high correlation of the fit parameters and the *k* range constraint on the number of independent points in the spectra, successive refinements were

Reproduced with permission of the copyright owner. Further reproduction prohibited without permission.

made by keeping some parameters constant while varying others. Again the values obtained for all three spectra were consistently similar. The best spectrum fit was obtained by a combination of FeS_2 (30%) and Li_2FeS_2 (70%) starting structures, in which the distances of Li_2FeS_2 were allowed to vary (Fig. 35). The best fit values for the first Fe-S distance in Li_2FeS_2 thus obtained were 2.31 ± .01 A. This is a significant deviation from the first Fe-S (2.37 A) reported for crystalline Li_2FeS_2 [84]. The second peak is fit to a Fe-Fe interaction at 2.73 A. Thus the main scattering contribution in this group of spectra is due to a Fe environment isostructural to Li_2FeS_2 but with a shorter atomic distances, possibly amorphous Li_xFeS_2. There is a possibility that the reported crystallographic distances are incorrect and the compound is in fact Li_2FeS_2. This distorted tetrahedral Fe environment of this structure can be associated with the sharp rise in the pre-edge feature. The lack of longer range order, i.e. peaks in the spectrum, may be due to random Li site occupation for this non-stoichiometric Li_xFeS_2. The pyrite contribution to the first shell although small is required by the fit in order to obtain a reasonable distortion factors for all scattering paths. The absence of longer range peaks due to the pyrite may be explained by the previously mentioned

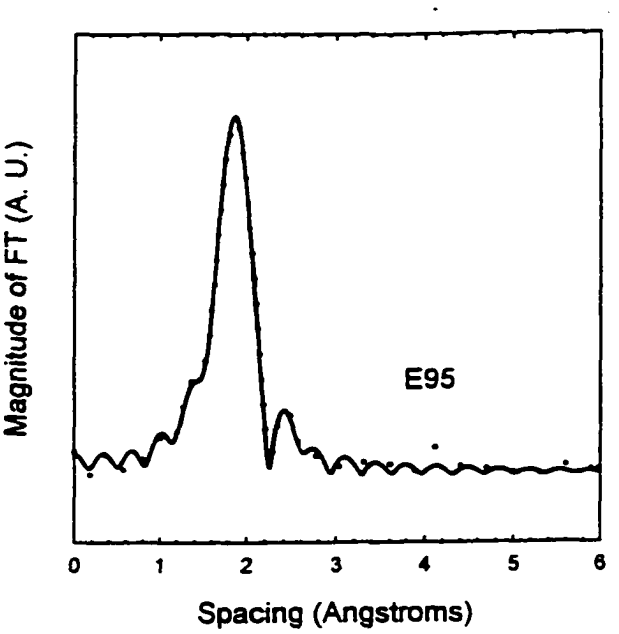

Figure 36
Simulation fit to the FTA of a representative "low" lithium content cathode sample. The peak positions and relative amplitudes are similar to those of Li_2FeS_2.

Reproduced with permission of the copyright owner. Further reproduction prohibited without permission.

$Fe_{1-x}S$ phase which in also considered to be amorphous.

3.6 H-ion Batteries [85]

A new type of H ion battery, incorporating a solid MnSO4*H2O based cathode and polymer electrolyte shows considerable promise as a rechargeable energy source. The battery was developed by Niles Fleisher at ECR Ltd, Rehovot, Israel.

The microscopic changes occurring in a the cathode are not well understood. What is known, however, is that they are more complex than chemical intercalation/deintercalation of ions into a host, such as in most Li ion batteries, for example. The cathode substrate possibly undergoes a wide range of intermediate chemical reactions in which the Mn oxidation state changes in accordance with the transfer of H ions between the cathode/electrolyte interface. The situation is complicated by the reactions at the interface, as well as inside the electrolyte. We have used x-ray absorption spectroscopy in order to focus on the Mn component and address the following questions:

1.What are the Mn oxidation states upon charging, and can we say something about the probable intermediate Mn compounds being formed?

2. Is charge conserved from the point of view of the capacity of the cathode, i.e. do changes in Mn oxidation state exclude a possible "bottle-necking". In other words, are all the thermodynamically allowed oxidation states reached?

3. What are the structural changes in the cathode during the charge/discharge cycle?

4. Is the cathode structurally stable after heavy cycling?

Reproduced with permission of the copyright owner. Further reproduction prohibited without permission.

1. **Experiment**

Individual battery cells were cycled using a simple charging circuit (Fig. 37).The current in the circuit was maintained less than 10mA. Three identically prepared cells were subjected to one of the following regimes:

- charge (up to 8.1 mAh), Vcell=2.0V

-discharge, Vcell =0.7V

-charge-discharge (Vcell=0.7V)-charge (q=7.54mAh, Vcell=1.35V)

A fourth cell, prepared in the uncharged state was used a reference. Several other highly cycled cells in discharge were also measured spectroscopically.

After cycling the cells, each one was immediately taken apart and thin samples (around 20-30 mg) were prepared by rolling the cathode material between wax paper. The samples were measured in transmission at beamline X23-B at NSLS, Brookhaven. The absorption in the samples in the Mn K-edge range, 6200-7400 eV, was recorded for each cell, various Mn compounds, and a simultaneous reference (Mn foil) for energy calibration.

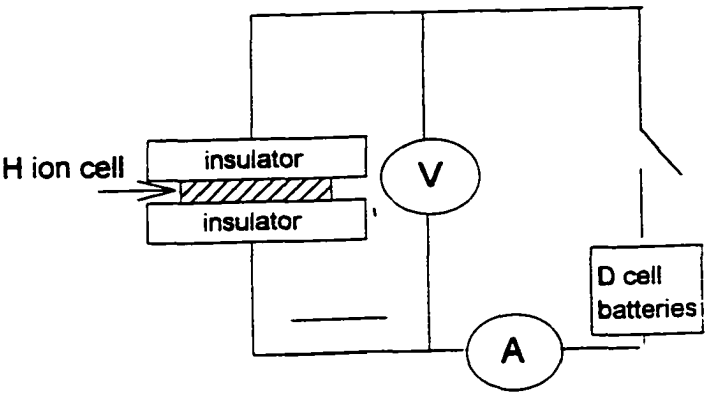

Figure 37 Charge circuit for quasi-*in-situ* XAS measurement of H-ion cell's Mn K-edge. The charge in the cathodes was calculated as

$$q=\int_{t_0}^{t_1} i(t)dt$$

2. **NEXAFS and EXAFS Analysis**

Reproduced with permission of the copyright owner. Further reproduction prohibited without permission.

Fig. 38 shows the near edge spectra of the three H ion cells measured quasi-*in-situ*. The changes in the main post-edge peak (white-line) are apparent, as well as the main edge shift (~ 1 eV) upon charging. The shift is obviously due to the increased oxidation state of the Mn^{2+} ion in $MnSO_4$. The core electrons are subjected to less screening upon ejection. A measurement of this effect was performed on stoichiometric Mn compounds in which Mn oxidation state ranges from 0 through +7. The compounds are dissimilar in terms of Mn-coordination, thus the fine pre-edge peak due to a 1*s*-*nd* type transitions have different broadening, position and are absent altogether in the case of metallic Mn^0. The position of the "true" edge position is somewhat debatable and is usually regarded as being masked by pre-edge transitions. We have chosen a consistent set of points

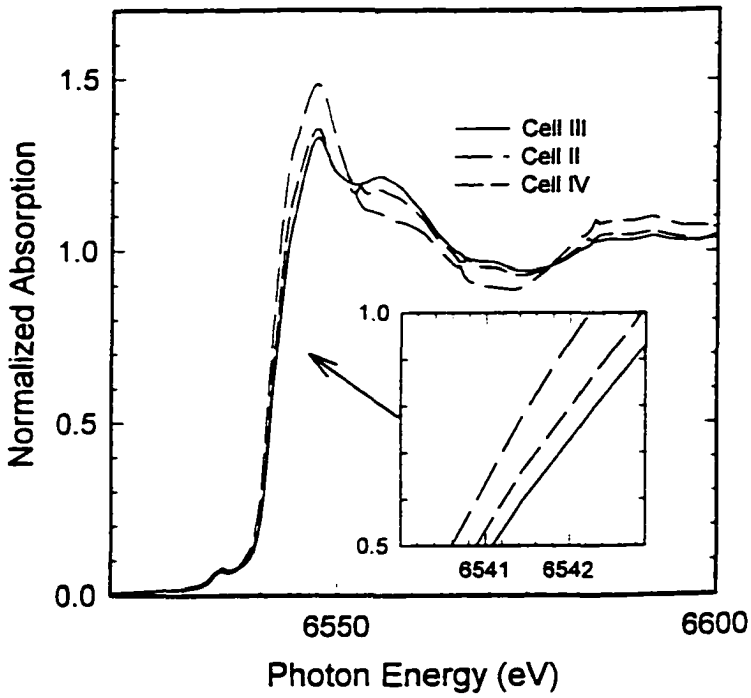

Figure 38 Mn K-edge NEXAFS of H⁺ ion cell cathodes. The inset shows the chemical edge shift as a result of cell charge.

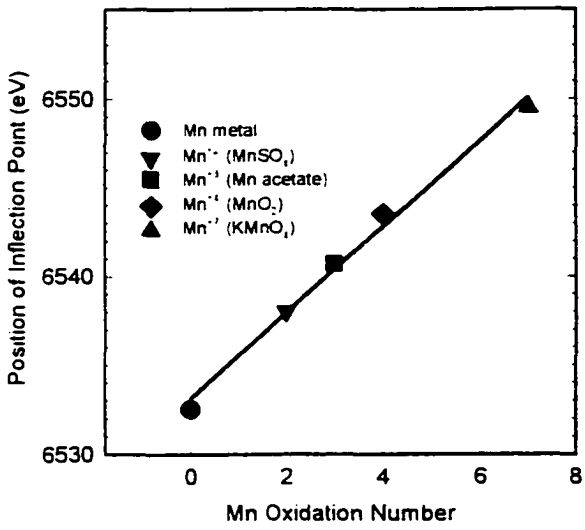

Figure 39 1*s* pre-edge peak shift measured for several different Mn compounds and linear regression showing shift as function of oxidation state.

Reproduced with permission of the copyright owner. Further reproduction prohibited without permission.

corresponding to the inflection of the first derivative of the spectra right after the identifiable pre-edge peak. Fig. 39 demonstrates that shifts in this point can be easily linearly related to oxidation state. The error bars are somewhat dependent on density of points and smoothness of the reference spectra in that region but the slope of the regression isn't. Using that as a scale we determined the average Mn valence in the cycled cells to be the ones given in Table 6.

Cell	Edge Simulation	Pre-Edge Shift
Cell IV (charge)	2.39 ± 0.2	2.38 ± 0.2
Cell II (ch./disch.)	2.12 ± 0.2	2.11 ± 0.2
Cell III(ch./disch./ch.)	2.33 ± 0.2	2.31 ± 0.2

Table 6. Average Mn valence abundances calculated from edge simulation and pre-edge shift

An alternative way of determining valence abundance is a least-squares fit of the cell edges in terms of empirical reference compound spectra. The assumption is that the main contributions to the fit will come from the main edge for which a correlation between the edge position and Mn oxidation state has been established. Smaller contributions will arise from the white line region. The latter exhibits some

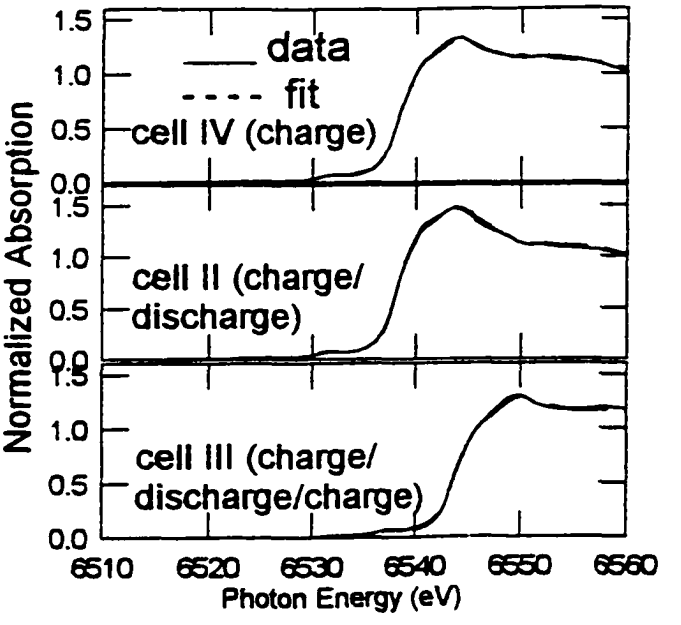

Figure 40 Mn K-edge simulation of H-ion battery cathode edge spectra based on fit to "standard edges".

Reproduced with permission of the copyright owner. Further reproduction prohibited without permission.

degree of correlation to oxidation state, i.e. relative increase in the WL intensity with lowering of the Mn valence. Of course the exact shapes will be influenced by details of the chemical bonding, but those can be neglected to a first approximation. Fig. 40 shows the fits of cells 2. 3 and 4 along with the best fit values. Using these percentages and doing a simple back calculation we get the same (within a small uncertainty) average oxidation state as from the edge shift.

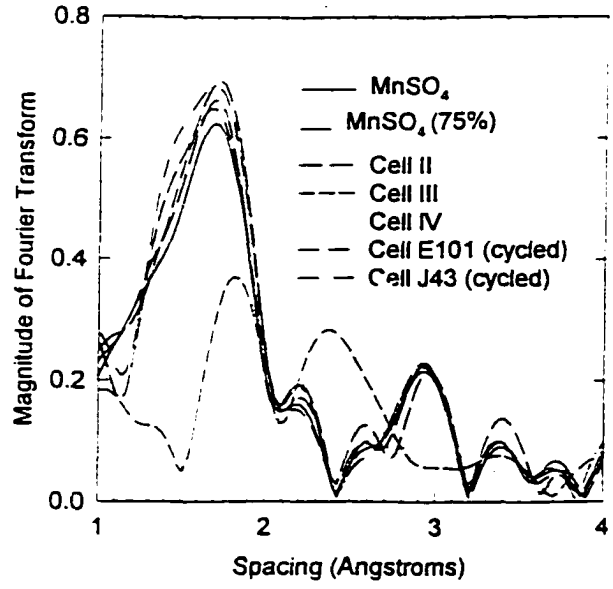

Figure 41 K-edge FTAs of different Mn compounds. charged cells and heavily cycled cathode materials (E 101 and J 43)

These calculations, along with the ones of balancing accumulated charge in the cathode with the amount of active material (MnSO4*H2O) indicate that the correct amount of Mn (within the uncertainty) is being oxidized as H^+ ions move across the interface. What doesn't seem to occur is the creation of Mn^{+7} (it is certainly less than 1%) which would increase the cell capacity, and which is also , according to preliminary calculations, energetically favorable considering the list of possible step reaction candidates. A small Mn^{4+} seems to be retained after discharge, and is favored upon charging again (Fig. 7), therefore the associated compound (possibly MnO_2) appears to be more stable[1] than the Mn^{3+} (possibly Mn_2O_3). So far, in examining the near-edge we were concerned with electronic-changes, leading to different oxidation states. The EXAFS spectra supply structural information. The EXAFS analysis of the cycled

[1] Private discussions with Jim McBreen have let us to believe that this may not be the case, due the instability of M^{+4} at room temperature. Further investigations will be needed in order to determine this result.

Reproduced with permission of the copyright owner. Further reproduction prohibited without permission.

cathodes reveals that the structure of the non-cycled cathode, cell 2(discharge) and two heavily cycled cell cathodes (40 and 80 cycles, discharged) are almost identical. Fig.41 shows the Fourier transformed amplitudes in position space of the EXAFS data (background subtracted and converted to *k*-space). The peaks correspond to individual coordination shell distances (or shell overlaps, the resolution is not great due to high frequency non-structural components present).

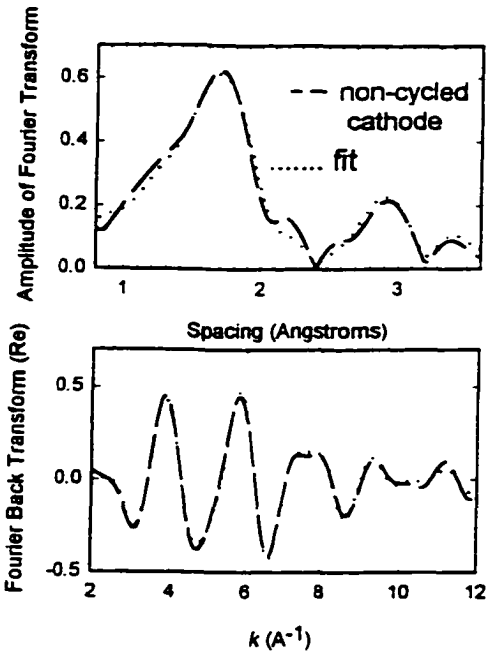

Figure 42 Least-squares fit simulation based on FEFF functions of active cathode material. The local structure was assumed to be $MnSO_4$ -like.

The first peak is the oxygen shell. Fitting these spectra with a theoretically calculated (Feff 6.01) based on the atomic positions of crystalline MnSO4 (Fig. 42), assumed to be similar the hydrate, gives very good results, independent of data weighting and range. We are led to conclude that the Mn2+ is almost entirely in the crystalline state of the starting material and this is retained after at least 80 cycles. Small impurities may be present (there is an indication for this from x-ray diffraction analysis and also from a somewhat greater uncertainty in the fitting).

The RDF spectra of cells 3 and 4 are very similar. They differ, however from the previous set, indicating structural phase transitions. Attempts to fit these with the MnSO4(*H2O) crystalline model spectrum fail. The first peak appears to have a different coordination (assuming it is due to an oxygen shell and chemical transferability of the model). The relative shape and position of the peaks is much more dependent of weighting and windowing than in the previous examples. There is also a obvious lack of higher order peaks, strongly suggesting a possible amorphousation of the

Reproduced with permission of the copyright owner. Further reproduction prohibited without permission.

hydrated sulfate or actual chemical change. Whether the latter is energetically feasible needs to be determined.

Reproduced with permission of the copyright owner. Further reproduction prohibited without permission.

Summary

X-ray absorption studies were undertaken as part of a collaborative spectroscopy investigation effort of new battery materials which include lithiated transition-metal oxide cathodes. A new type of hydrogen ion conducting battery was also studied with quasi-*in-situ* x-ray absorption measurements. Our analysis has revealed some new facts regarding the local structural and electronic changes in these systems upon charge/discharge.

NEXAFS analysis of the spectra of $Li_{1-x}CoO2$ secondary battery cathodes revealed that the addition of Li proceeds is strongly correlated to the increase in electronic charge on the Co ion. A structural phase transition is confirmed for $x = 0.5$. The presence of Mn^{+2} is detected in the conventionally made $LiMnO_2$ cathodes but not in ones prepared according to the new ADL process.

$Li_xV_6O_{13}$ cathode material, where $0 \leq x \leq 6$, was measured using x-ray absorption, EPR and NMR techniques. The intercalation mechanism involves a conversion of V^{+5} to V^{+4} in V_6O_{13} until the composition $Li_2V_6O_{13}$ is reached. Further addition of lithium is accompanied by the conversion of V^{+4} to V^{+3} until $Li_8V_6O_{13}$ is reached. The process is complicated and involves structural phase changes and increasing structural disorder within the multi-phase system as Li concentration is increased.

Studies of $LiNi/CoO_2$ intercalation cathodes prepared by a novel sol-gel technique suggests that although the partial substitution of Co for Ni stabilizes the system by removing Ni^{+2}, a Jahn-Teller type structural distortion in the predominantly Ni^{+3} system persists.

In-situ EXAFS measurements of the pyrite cathode in a new $Li/CPE/FeS_2$ battery

Reproduced with permission of the copyright owner. Further reproduction prohibited without permission.

showed two distinct environments of the Fe ion, which were interpreted as those of metallic Fe and residual FeS_2 at high lithium concentration, and Li2FeS_2 and residual FeS_2 low lithium concentration. The formation of FeS was not detected.

A new type of hydrogen ion battery incorporating a $MnSO_4*H_2O$ based cathode and polymer electrolyte was also studied. Heavily cycled and discharged cathodes showed an almost identical Mn local structure to that of single cycled ones. The Mn environment becomes very different in the charged cathodes, due to a highly reversible chemical change. Formation of Mn+4 at the expense of Mn+3, upon charging is an unexpected result. Mn+7 does not appear to be created in this process.

This information coupled with other results in this growing sub-field of material science has contributed to a more comprehensive understanding of the structure and physical and chemical properties of these new materials.

This work also allowed us to test the viability of employing complimentary spectroscopies, i.e., NMR and EPR which mostly probe the electronic states of these battery systems, and X-ray absorption which can be used to investigate local structrure and electronic properties. Our conclusion is that this type of systematic collaborative research is important and should be developed further, especially in view of the growing complexity, both chemical and structural of new energy materials.

Reproduced with permission of the copyright owner. Further reproduction prohibited without permission.

References

1. D. A. Scherson, The Electrochemical Society *Interface*, Fall 1996

2. Gauthier, M. et. al. in *Polymer Electrolyte Reviews*, Elsevier Science Publishers (1989)

3. D. W. Murphy and P.A. Christian, *Science*, **205**, 4407 (1979)

4. C. Julien and G. Nazri, *Solid State Batteries: Materials Design and Optimization*, Kluwer Academic Publishers, 1994

5. Solin, S. A., Adv. Chem. Phys., **49**, 455-532 (1982)

6. Dresselhaus, M. S. and Dresselhaus, G., Adv. Phys., **30**, 139-326 (1981)

7. McKinnon, W R., *Solid State Electrochemistry*, Ed. P.G. Bruce, Cambrige University Press, 1995

8. Clarke, R., Caswell, N., and Solin, S. A., Phys. Rev. Lett., **47**, 1407-10 (1979)

9. Moline, P. Trichet, L., Rouxel, J . Berthier, C., Chabre, Y. and Segransan, P., J. Phys. Chem. Solids, **45**, 105-12 (1984)

10. Shannon, R. D., Acta Crystallographica A, **32**, 751-67 (1976)

11. Py, M. A. and Haering, R. R., Can. J. Phys., **61**,76-84, 1983

12. Zaanen, J., Sawatzky, G. A. and Allen, J. W., Phys. Rev. Lett., **55**, 418-21 (1985)

13. Rouxel, J., *Solid State Ionics*, Eds. G. Nazri, R. F. Huggins, and D. F. Shriver, Materials Research Society, Pittsburgh, pp. 431-42, 1989

14. Umrigar, C. Ellis, D. E., Wang, D E., Krakauer, H. and Posternak, M., Phys. Rev. B, **26**, 4395-50, 1982

15. Mott, N. F. and Davis, E. A., *Electronic Processes in Non-Crystalline Materials*, Claredon Press, Oxford, 1979

16. Hill, M. D. and Egdell, R. G., J. Phys. C, **16**, 6205-20 (1983)

17. Chevrel, R. and Sergent, M., *Superconductivity in Ternery Compounds I*, Eds. O. Fischer and M. B. Maple, Springer-Verlag, Berlin, pp. 25-86 (1982)

Reproduced with permission of the copyright owner. Further reproduction prohibited without permission.

18. Tarascon, J. M., DiSalvo, F. J., Chen, C. H., Carroll, P. J., Walsh, M. and Rupp, L., J. Solid State Chem., **58**, 290-300, 1985

19. Hulliger, F., *Structural Chemistry of Layer- Type Phases*, Reidel, Dordrecht, 1976

20. Whittingham, M. S. and Gamble, F. R., Mat. Res. Bull. **10**, 362-72, 1975

21. Tigchelaar, C., Wiegers, G. A. and van Bruggen, C. F., Revue de Chimie Minerale, **19**, 352-9 (1982)

22. Dahn, J. R, von Sacken, U. and Michal, C. A., Solid State Ionics, **44**, 87-97, 1990b

23. Murphy, D. W., Christian, P.A., DiSalvo, F. J.,Carides, J. N., and Waszczak, J. V., J. Electrochem. Soc., **128**, 2053-60 (1981)

24. Cava, R. J., Santoro, A., Murphy, D. W., Zahurak, S., Fleming, R. M., Marsh, P. and Roth, R. S., Journal of Solid State Chimistry, **65**, 63-71, 1986

25. Nohl, H., Klose, W. and Andersen, O. K., *Superconductivity in Ternary Compounds I*, Eds. O. Fischer and M. B. Maple, Springer-Verlag, Berlin, 1982

26. Cava, R. J., Santoro, A. Murphy, D W., Zahurak, S. and Roth, R. S., J. Solid State Chem., **42**, 251-62, 1982

27. Murphy, D. W., Christian, P. A., DiSalvo, F. J., Carides, J. N., and Waszczak, J. V., J. Electrochemical Society, **128**, 2053-60

28. McKinnon, W. R. and Haering, R. R., *Modern Aspects of Electrochemistry*, Vol. 15, Eds. R. E. White, J. O'M. Bockris and B. E. Conway, Plenum, New York, pp.235-304

29. Dahn, J. R. and Haering, R. R., Can. J. Phys., **61**, 1093-8, 1983

30. Dahn, J. R. and McKinnon, W. R., Phys. Rev. **B**, 32, 3003-5, 1985

31. Kittel, C., *Introduction to Solid State Physics*, 4th edition, Wiley, New York, 1971

32. P. A. Lee, P H. Citrin, P. Eisenberger, and B.M. Kincaid, Reviews of Modern Physics, Vol. 53, No.4, Part I, October 1981

33. E. Sevillano, H. Meuth, and J. J. Rehr, Phys. Rev. B, **20**, 4908 (1979)

34. Edward A. Stern, in X-ray Absorption: Principles, Applications, Techniques of EXAFS, SEXAFS and XANES, K.C. Konigsberger and R. Prins (Eds.) Wiley-interscience, Chemical Analysis, **92**, 21 (1988)

Reproduced with permission of the copyright owner. Further reproduction prohibited without permission.

35. Durham, P. J., in The Electronic Structure of Complex Systems, P. Phariseau and W. Temmerman (Eds.), Plenum, New York, 1984

36. J. E. Müller, *EXAFS and Near Edge Structure III*, ed. by K.O. Hodgson, B. Hedman, J. E. Penner-Hahn, Springer Proc. Phys., Vol.2 (Springer, Berlin, Heidelberg 1984) p. 7

37. Parrat, L. G., Rev. Mod. Phys., **31**, 616 (1959)

38. Cauchois, Y., Mott, N. F, Philos. Mag., **40**, 1260 (1949)

39. Richmyer, F. K., Barnes, S. W., Ramberg, E., Phys. Rev. **46**, 843 (1934)

40. Agarwal, B. K., Verma, L. P., J. Phys. C **3**, 535, 1070

41. Ovsyannikova, I. A., Batsanov, S. S., Nanonova, L. I., Batsanova, L. R., Nekrasova, E. A., Bull. Acad. Sci. USSR, Phys. Ser. **31**, 936, (1967)

42. Dey, A. K., Agarwal, B. K., J. Chem. Phys. **59**, 1397, 1973

43. A. R. Chetal, P. Mahto and P.R. Sarode, J. Phys. Chem. Solids **49**, 279 (1988)

44. McDowell, R. A. *et al.*, Rev. Sci. Inst., **59**, 843-852

45. Greaves, G. N., and Raoux, D., *Structrure of Non-Crystalline Materials II*, Taylor and Francis, London, pp. 55-80, 1983

46. Heald, S. M., Keller, E., and Stern, E. A., Phys. Lett., **103A**, 155-158, 1984

47. Stöhr, J., Kollin, E. B., Fischer, D. A. Hastings, J.B., Zaera, F., and Sette, F., Phys. Rev. Lett., **55**, 468-1471

48. Guo T. and denBoer, M. L., Phys. Rev. **B31**, 6233-6237, 1985

49. The UWXAFS programs are copyrighted and licensed by the University of Washington. Contact E. A. Stern for further information.

50. J. J. Rehr, R. C. Albers, and S. I. Zabinsky, Phys. Rev. Lett. **69**, 3397 (1992), and *Ab initio Multiple-Scattering X-ray Absorption Fine Structure and X-ray Absorption Near Edge Structure Code*, Copyright 1992, 1993, FEFF Project, Department of Physics, FM-15 University of Washington, Seattle, WA 98195.

51. M. Newville, et. al., Physical Review B, Vol. 48, No. 13, 9825 (1993).

52. E. A. Stern, Physical Review B, Vol. 48, No. 13, 9825 (1993).

53. L. Brillouin, *Science and Information Theory*, Academic Press, New York, 1962

Reproduced with permission of the copyright owner. Further reproduction prohibited without permission.

54. M. Newville P Livins, Y. Yacoby, J.J Rehr, and E. A. Stern, Phys. Rev. **B47**, 14, 126 , 1993

55. J. J. Rehr, R. C. Albers, and S. I. Zabinsky, Physical Review Letters, Vol. 69, No. 23, 3397 (1992)

56. B. Ouyang, X. Cao, H. W. Lin, S Slane, S. Kostov, M L denBoer, and S. G. Greenbaum, Mat. Res. Soc. Symp. Proc. 369, 73 (1995)

57. Reimers, J. N., and Dahn, J. R . J Electrochem. Soc., Vol 139, No. 8, 1992

58. B. Ouyang, M. denBoer, D. Feuteux, A. Massucco, M. vanBuren, M. McLin, Mat. Res. Soc. Symp. Proc. 369, 73 (1995).

59. B. E. Conway, D. Qu and J. McBreen, in *Synchrotron Techniques in Interfacial Chemistry*, edited by C. A. Melendres and A. Tadjeddine (Kluwer Academic Publishers, Dordrecht, 1994), pp. 311-334.

60. M. Brown, R. E. Peirls and E. A Stern, Phys. Rev. B, **15**, 738 (1997).

61. P.E. Stallworth, S. Kostov, M L denBoer, S.G. Greenbaum and C. Lampe-Onnerud, J. Appl. Phys. **83** (3) 1247-1255, 1998

62. R. Tossici, R. Marassi, M. Berrtoni, S. Stizza and G. Pistoia, Solid State Ionics **67**, 77 (1993).

63. J. Wong, F.W. Lytle, R.P Messmer, and D H. Mayolotte, Phys. Rev. B **30**, 5596 (1984).

64. B. K. Agarwal, *X-ray Spectroscopy*, Second Edition (Springer, New York, 1991).

65. R. D. Leapman, L. A. Grunes, and P L. Fejes, Phys. Rev B **26**, 614 (1982).

66. B. Hedman, J.E. Penner-Hahn, and K.O Hodgson: In *EXAFS and Near Edge Structure III*, ed. by K.O. Hodgson, B.Hedman, and J.E. Penner-Hahn, Springer Proc. Phys., Vol. **2**. (Springer, Berlin, Heidelberg, 1984) p.64.

67. A. F. Wells, *Structural Inorganic Chemistry*, Fifth Edition, (Clarendon Press, Oxford 1984).

68. K.-A. Wilhelmi, K.Waltersson, and L. Kihlborg, Acta Chem. Scand. **25**, 2675 (1971).

69. B. K. Teo, *Extended X-Ray Absorption Fine Structure (EXAFS) Spectroscopy: Techniques and Applications*, Plenum Press, 1981

70. Christina Lampe-Önnerud, Ph.D Thesis, Institute of Chemistry, Uppsala University, 1995

Reproduced with permission of the copyright owner. Further reproduction prohibited without permission.

71. S. Passerini, W H. Smyrl, M. Berrettoni, R. Tossici, M. Rosolen, R. Marassi, F. Decker, Solid State Ionics **90**, 5 (1996)

72. E. Plichta, S. Slane, M. Uchiyama, M. Salomon, D. Chua, W. B. Ebner, and H. W. Lin, J. Electrochem. Soc. **136**, 1865 (1986)

73. A. Abragam and B. Bleaney, *Electron Paramagnetic Resonance of Transition Ions* (Dover, New York, 1986).

74. S. Kostov, Y. Wang, M. L. denBoer, S. Greenbaum, Prashant N. Kumta and C.C. Chang, Mat. Res. Soc. Symp Proc. 1997

75. J. J. Rehr, R. C. Albers, and S. I. Zabinsky, Phys. Rev. Lett. **69**, 3397 (1992), and *Ab initio Multiple-Scattering X-ray Absorption Fine Structure and X-ray Absorption Near Edge Structure Code*, Copyright 1992, 1993, FEFF Project, Department of Physics, FM-15 University of Washington, Seattle, WA 98195.

76. L. D. Dyer, B. S. Borie, Jr., and G. P. Smith, J. Am. Chem. Soc. **76**, 1499 (1954).

77. A. N. Mansour and C. A. Melendres, J. Phys. Chem., **102**, issue 002, 1998.

78. A. R. Chetal, P Mahto and P R. Sarode, J Phys. Chem. Solids **49**, 279 (1988)

79. I. Pickering, G. George, J. Lewandowski, and A. Jacobson, J. Am. Chem. Soc., **115**, 4144 (1993)

80. A. Rougier, C. Delmas , and A Chadwick, Sol. State Comm. **94**, 123 (1995).

81. S. Kostov, M. denBoer E. Strauss, D. Golodnitsky, E. Peled and S.G. Greenbaum to be submitted for publication

82. D.A. Tryk *et. al.*, J. Phys. Chem. 99, 3732-3735 (1995).

83. A. Iida *et. al.*, Jpn J. Appl. Phys , Suppl **32**, 2 160 (1993)

84. Batchelor, R. J., Einstein, F W B and Jones, C. H. W., Phys. Rev. B, **37**, 3699, (1988)

85. S. Kostov, M. L. denBoer, S. Greenbaum, N. A. Fleisher J. Lang, E. Rosh-Chodesh, to be submitted for publication

Reproduced with permission of the copyright owner. Further reproduction prohibited without permission.

IMAGE EVALUATION
TEST TARGET (QA-3)

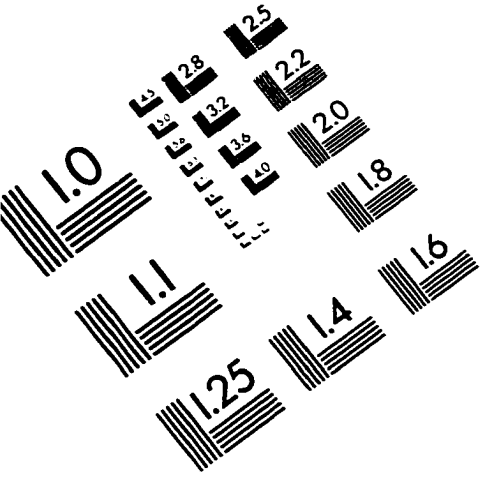

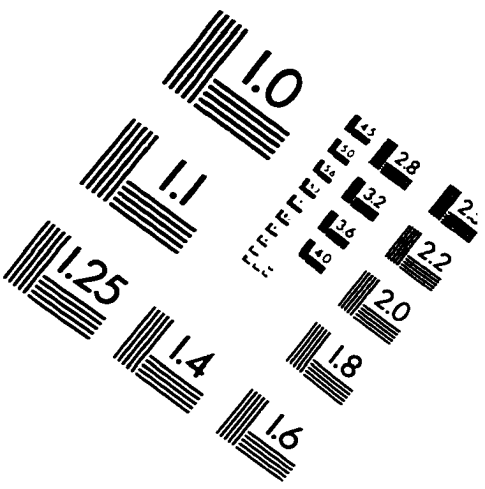

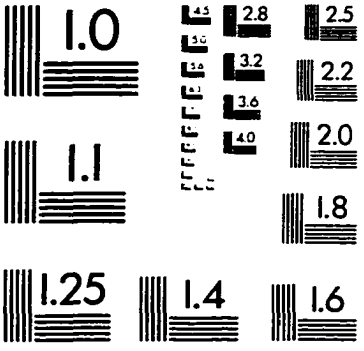

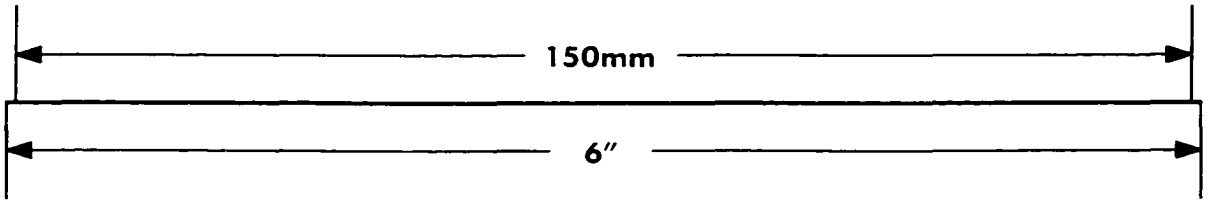

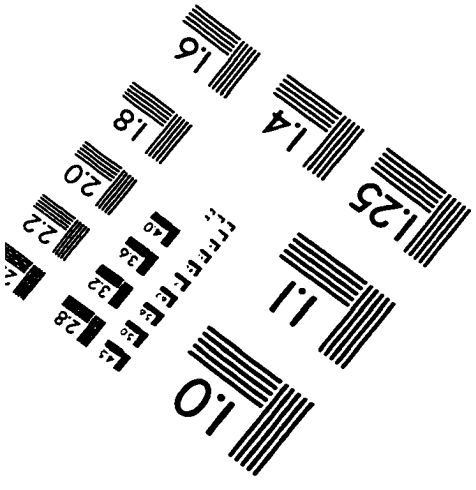

APPLIED IMAGE, Inc
1653 East Main Street
Rochester, NY 14609 USA
Phone: 716/482-0300
Fax: 716/288-5989

© 1993, Applied Image, Inc., All Rights Reserved

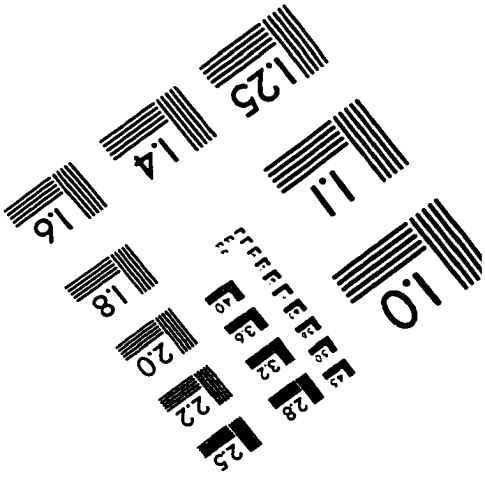

Reproduced with permission of the copyright owner. Further reproduction prohibited without permission.